The Astrophysical Journal Letters, 954:L4 (17pp), 2023 September 1 https://doi.org/10.3847/2041-8213/ace5a0

Hidden Little Monsters: Spectroscopic Identification of Low-mass, Broad-line AGNs at $z > 5$ with CEERS

Dale D. Kocevski[1], Masafusa Onoue[2,3,37], Kohei Inayoshi[2], Jonathan R. Trump[4], Pablo Arrabal Haro[5], Andrea Grazian[6], Mark Dickinson[5], Steven L. Finkelstein[7], Jeyhan S. Kartaltepe[8], Michaela Hirschmann[9], James Aird[10], Benne W. Holwerda[11], Seiji Fujimoto[7,12,13,38], Stéphanie Juneau[14], Ricardo O. Amorín[15,16], Bren E. Backhaus[4], Micaela B. Bagley[7], Guillermo Barro[17], Eric F. Bell[18], Laura Bisigello[6,19], Antonello Calabrò[20], Nikko J. Cleri[21,22], M. C. Cooper[23], Xuheng Ding[3], Norman A. Grogin[24], Luis C. Ho[2,25], Taylor A. Hutchison[26,39], Akio K. Inoue[27,28], Linhua Jiang[2,25], Brenda Jones[29], Anton M. Koekemoer[24], Wenxiu Li[2], Zhengrong Li[2], Elizabeth J. McGrath[1], Juan Molina[2,30], Casey Papovich[21,22], Pablo G. Pérez-González[31], Nor Pirzkal[32], Stephen M. Wilkins[33,34], Guang Yang[35,36], and L. Y. Aaron Yung[26,39]

[1] Department of Physics and Astronomy, Colby College, Waterville, ME 04901, USA; dale.kocevski@colby.edu
[2] Kavli Institute for Astronomy and Astrophysics, Peking University, Beijing 100871, People's Republic of China
[3] Kavli Institute for the Physics and Mathematics of the Universe (Kavli IPMU, WPI), The University of Tokyo, Chiba 277-8583, Japan
[4] Department of Physics, 196 Auditorium Road, Unit 3046, University of Connecticut, Storrs, CT 06269, USA
[5] NSF's National Optical-Infrared Astronomy Research Laboratory, 950 N. Cherry Ave., Tucson, AZ 85719, USA
[6] INAF–Osservatorio Astronomico di Padova, Vicolo dell'Osservatorio 5, I-35122, Padova, Italy
[7] Department of Astronomy, The University of Texas at Austin, Austin, TX 78712, USA
[8] Laboratory for Multiwavelength Astrophysics, School of Physics and Astronomy, Rochester Institute of Technology, 84 Lomb Memorial Drive, Rochester, NY 14623, USA
[9] Institute of Physics, Laboratory of Galaxy Evolution, Ecole Polytechnique Fédérale de Lausanne (EPFL), Observatoire de Sauverny, 1290 Versoix, Switzerland
[10] Institute for Astronomy, University of Edinburgh, Royal Observatory, Edinburgh EH9 3HJ, UK
[11] University of Louisville, Department of Physics and Astronomy, 102 Natural Science Building, Louisville, KY 40292, USA
[12] Cosmic Dawn Center (DAWN), Jagtvej 128, DK-2200 Copenhagen N, Denmark
[13] Niels Bohr Institute, University of Copenhagen, Lyngbyvej 2, DK-2100 Copenhagen Ø, Denmark
[14] NSF's NOIRLab, 950 N. Cherry Ave., Tucson, AZ 85719, USA
[15] Instituto de Investigación Multidisciplinar en Ciencia y Tecnología, Universidad de La Serena, Raul Bitrán 1305, La Serena 2204000, Chile
[16] Departamento de Astronomía, Universidad de La Serena, Av. Juan Cisternas 1200 Norte, La Serena 1720236, Chile
[17] Department of Physics, University of the Pacific, Stockton, CA 90340, USA
[18] Department of Astronomy, University of Michigan, 1085 S. University Ave, Ann Arbor, MI 48109-1107, USA
[19] Dipartimento di Fisica e Astronomia "G. Galilei," Universitá di Padova, Via Marzolo 8, I-35131 Padova, Italy
[20] Osservatorio Astronomico di Roma, via Frascati 33, Monte Porzio Catone, Italy
[21] Department of Physics and Astronomy, Texas A&M University, College Station, TX 77843-4242, USA
[22] George P. and Cynthia Woods Mitchell Institute for Fundamental Physics and Astronomy, Texas A&M University, College Station, TX 77843-4242, USA
[23] Department of Physics & Astronomy, University of California, Irvine, 4129 Reines Hall, Irvine, CA 92697, USA
[24] Space Telescope Science Institute, 3700 San Martin Dr., Baltimore, MD 21218, USA
[25] Department of Astronomy, School of Physics, Peking University, Beijing 100871, People's Republic of China
[26] Astrophysics Science Division, NASA Goddard Space Flight Center, 8800 Greenbelt Rd., Greenbelt, MD 20771, USA
[27] Waseda Research Institute for Science and Engineering, Faculty of Science and Engineering, Waseda University, 3-4-1, Okubo, Shinjuku, Tokyo 169-8555, Japan
[28] Department of Physics, School of Advanced Science and Engineering, Faculty of Science and Engineering, Waseda University, 3-4-1, Okubo, Shinjuku, Tokyo 169-8555, Japan
[29] Department of Physics and Astronomy, University of Maine, Orono, ME 04469-5709, USA
[30] Department of Space, Earth and Environment, Chalmers University of Technology, Onsala Space Observatory, SE-439 92 Onsala, Sweden
[31] Centro de Astrobiología (CAB), CSIC-INTA, Ctra. de Ajalvir km 4, Torrejón de Ardoz, E-28850, Madrid, Spain
[32] ESA/AURA Space Telescope Science Institute, USA
[33] Astronomy Centre, University of Sussex, Falmer, Brighton BN1 9QH, UK
[34] Institute of Space Sciences and Astronomy, University of Malta, Msida MSD 2080, Malta
[35] Kapteyn Astronomical Institute, University of Groningen, P.O. Box 800, 9700 AV Groningen, The Netherlands
[36] SRON Netherlands Institute for Space Research, Postbus 800, 9700 AV Groningen, The Netherlands
Received 2023 February 10; revised 2023 June 28; accepted 2023 June 28; published 2023 August 24

Abstract

We report on the discovery of two low-luminosity, broad-line active galactic nuclei (AGNs) at $z > 5$ identified using JWST NIRSpec spectroscopy from the Cosmic Evolution Early Release Science (CEERS) survey. We detect broad Hα emission in the spectra of both sources, with FWHM of 2060 ± 290 km s^{-1} and 1800 ± 200 km s^{-1}, resulting in virial black hole (BH) masses that are 1–2 dex below those of existing samples of luminous quasars at $z > 5$. The first source, CEERS 2782 at $z = 5.242$, is 2–3 dex fainter than known quasars at similar redshifts and

[37] Kavli Astrophysics Fellow.
[38] Hubble Fellow.
[39] NASA Postdoctoral Fellow.

was previously identified as a candidate low-luminosity AGN based on its morphology and rest-frame optical spectral energy distribution (SED). We measure a BH mass of $M_{\rm BH} = (1.3 \pm 0.4) \times 10^7\, M_\odot$, confirming that this AGN is powered by the least massive BH known in the Universe at the end of cosmic reionization. The second source, CEERS 746 at $z = 5.624$, is inferred to be a heavily obscured, broad-line AGN caught in a transition phase between a dust-obscured starburst and an unobscured quasar. We estimate its BH mass to be in the range of $M_{\rm BH} \simeq (0.9\text{–}4.7) \times 10^7\, M_\odot$, depending on the level of dust obscuration assumed. We perform SED fitting to derive host stellar masses, $M_\star$, allowing us to place constraints on the BH–galaxy mass relationship in the lowest mass range yet probed in the early Universe. The $M_{\rm BH}/M_\star$ ratio for CEERS 2782, in particular, is consistent with or higher than the empirical relationship seen in massive galaxies at $z = 0$. We examine the narrow emission line ratios of both sources and find that their location on the BPT and OHNO diagrams is consistent with model predictions for moderately low metallicity AGNs with $Z/Z_\odot \simeq 0.2\text{–}0.4$. The spectroscopic identification of low-luminosity, broad-line AGNs at $z > 5$ with $M_{\rm BH} \simeq 10^7\, M_\odot$ demonstrates the capability of JWST to push BH masses closer to the range predicted for the BH seed population and provides a unique opportunity to study the early stages of BH–galaxy assembly.

Unified Astronomy Thesaurus concepts: Quasars (1319); Supermassive black holes (1663); High-redshift galaxies (734); Active galactic nuclei (16)

1. Introduction

With the advent of wide-field quasar surveys such as those carried out by the Sloan Digital Sky Survey (SDSS; Fan et al. 2001; Jiang et al. 2016), Pan-STARRS1 (Bañados et al. 2016; Mazzucchelli et al. 2017), CFHQS (Willott et al. 2007), DES (Reed et al. 2015), DESI (Yang et al. 2023), and SHELLQS (Matsuoka et al. 2016), hundreds of quasars have been discovered and characterized at $z > 5$ (Inayoshi et al. 2020; Fan et al. 2022), with the most distant found a mere 670 million years after the big bang (Wang et al. 2021). The supermassive black holes (SMBHs) that power these sources have masses of order $\sim 10^9\, M_\odot$, raising the question of how such systems were built in such a short amount of cosmic time.

Most theories involve Eddington-limited or possibly super-Eddington accretion onto seed black holes (BHs) that are predicted to form at $10 < z < 30$ and have masses that range from $\sim 10^2\, M_\odot$ (so-called "light seeds") to over $\sim 10^5\, M_\odot$ ("heavy seeds") with a continuous distribution (e.g., Inayoshi et al. 2020; Volonteri et al. 2021). The relative contribution of each seed type remains largely unconstrained by observations (Miller et al. 2015; Trump et al. 2015).

Most quasar surveys, which observe $\gtrsim 1000$ deg^2 down to ~ 20 mag, are sensitive to only the most luminous quasar populations ($\sim 10^{47}$ erg s^{-1} in bolometric luminosity, $L_{\rm bol}$). These ultrarare systems, which formed in biased regions of the early Universe, place limited constraints on the BH seed population, as they would have undergone sustained episodes of exponential growth, even for the most massive predicted seeds, thereby erasing the imprint of the initial seed mass distribution (e.g., Tanaka & Haiman 2009; Volonteri 2010). A complementary approach is to search for lower-luminosity quasars hosting SMBHs with masses closer to the predicted seed mass range at the earliest epochs possible (Somerville et al. 2008; Valiante et al. 2016; Ricarte & Natarajan 2018; Yung et al. 2021; Li et al. 2023). Several deep optical surveys have attempted to do this by reaching a dex fainter in luminosity (e.g., Willott et al. 2007, 2010; Matsuoka et al. 2016, 2022; Kim et al. 2018, 2020; Fujimoto et al. 2022); however, these samples are still far more luminous than what is observed in the nearby Universe ($L_{\rm bol} \sim 10^{43}\text{–}10^{44}$ erg s^{-1}; e.g., Greene & Ho 2007; Liu et al. 2018, 2019), biasing our understanding of early SMBHs toward the most massive and active populations (however, see also Mezcua et al. 2018).

Additional constraints on the seed mass distribution can be obtained by comparing the masses of high-redshift SMBHs to those of their host galaxies. In the local Universe, well-established scaling relationships exist between the mass of SMBHs and the bulge properties of their hosts (e.g., Magorrian et al. 1998; Ferrarese & Merritt 2000; Gebhardt et al. 2000; McConnell & Ma 2013; Sun et al. 2015). However, offsets from this relationship at higher redshift can help constrain models of early BH growth and their coevolution with galaxies (Hirschmann et al. 2010; Habouzit et al. 2022; Hu et al. 2022; Inayoshi et al. 2022a). Observational studies have produced mixed results in this regard, with several reporting that SMBHs become increasingly overmassive relative to their hosts with increasing redshift (e.g., Trakhtenbrot & Netzer 2010; Bennert et al. 2011; Park et al. 2015; Shimasaku & Izumi 2019; Ding et al. 2020; Neeleman et al. 2021), while other studies report no evolution in the local scaling relationship (e.g., Willott et al. 2017; Izumi et al. 2019; Suh et al. 2020). Pushing such studies to lower SMBH and host masses at high redshifts is expected to provide additional insight into the earliest seeds. Not only are lower-luminosity active galactic nuclei (AGNs) more representative of the normal BH population (Habouzit et al. 2022), but lower-mass hosts also have a relatively quiet merger history and so represent a robust "fossil record" of the initial BH seed mass distribution (Volonteri et al. 2008; Volonteri & Natarajan 2009).

JWST is expected to be a game changer on both fronts, allowing for the detection of lower-luminosity quasars and the light of their host galaxies out to the epoch of cosmic reionization. Since its launch, JWST has already revealed the host morphologies of X-ray and optically selected AGNs out to $z \sim 4$ (Ding et al. 2022b; Kocevski et al. 2023), detected the host light of a quasar at $z \simeq 6$ for the first time (Ding et al. 2022a), and identified a candidate faint quasar at $z \simeq 7.7$ (Furtak et al. 2023). Recently, Onoue et al. (2023, hereafter O23) reported a candidate low-luminosity AGN at $z \sim 5$ by exploiting the first NIRCam images of the Cosmic Evolution Early Release Science (CEERS) program. This AGN candidate, CEERS-AGN-z5-1, has a compact morphology and shows a rest-frame UV-to-optical spectral energy distribution (SED) that can be well explained by an unobscured quasar with $L_{\rm bol} = (2.5 \pm 0.3) \times 10^{44}$ erg s^{-1} and strong Balmer and [O III] emission lines. In addition, Carnall et al. (2023) recently reported the detection of broad Hα emission from a quiescent

galaxy at $z = 4.658$ using JWST, from which they measure the central SMBH mass of $M_{\rm BH} = 10^{8.7\pm0.1}\ M_{\odot}$.

Here we report on the detection of broad Hα emission from two $z > 5$ galaxies, including CEERS-AGN-z5-1, using NIRSpec data obtained as part of the second epoch of CEERS observations. The first source, CEERS 2782 at $z = 5.242$, was identified as a result of targeted follow-up of CEERS-AGN-z5-1, while the second source, CEERS 746 at $z = 5.624$, was found serendipitously while inspecting the spectra of galaxies with photometric redshifts of $z > 8$ in the literature.

We show that the SMBHs at the heart of these low-luminosity AGNs have masses 1–2 dex lower than existing samples of luminous quasars with BH mass estimates at $z > 5$. We also examine the emission-line ratios of both sources and place constraints on the relationship between SMBH and host mass in the lowest mass range yet probed in the early Universe. Our analysis is presented as follows: In Section 2, we describe the near-infrared imaging and spectroscopy used for this study. In Section 3, we discuss the properties of our sample. In Section 4, we outline our methodology for measuring the emission-line properties of our sample. Section 5 describes our results, and the implications of our findings are discussed in Section 6. We use vacuum wavelengths for all emission-line features, and, when necessary, the following cosmological parameters are used: $H_0 = 70\ {\rm km\ s^{-1}\ Mpc^{-1}}$, $\Omega_\Lambda = 0.7$, and $\Omega_m = 0.3$.

2. Observations and Data Reduction

CEERS is an early release science program that covers 100 arcmin^2 of the Extended Groth Strip (EGS) with imaging and spectroscopy using coordinated, overlapping parallel observations by most of the JWST instrument suite (S. Finkelstein et al. 2023, in preparation). CEERS is based around a mosaic of 10 NIRCam pointings, with six NIRSpec and eight MIRI pointings observed in parallel. Here we make use of NIRCam pointings 3 and 6, obtained on 2022 June 21, as well as NIRSpec pointing 4, obtained on 2022 December 21. In each NIRCam pointing, data were obtained in the short-wavelength (SW) channel F115W, F150W, and F200W filters and long-wavelength (LW) channel F277W, F356W, F410M, and F444W filters. The total exposure time for pixels observed in all three dithers was typically 2835 s per filter.

The NIRSpec observations were taken with the G140M/F100LP, G235M/F170LP, and G395M/F290LP $R \simeq 1000$ grating/filter pairs, as well as with the $R \simeq 30$–300 prism, providing a complete coverage of the 1–5 μm range with both configurations. The observation adopted a three-nod pattern, each of the nods consisting of a single integration of 14 groups (1036 s). The coadded spectra have a total exposure time of 3107 s in each spectral configuration. Targets for the microshutter array (MSA) configuration included sources selected using the NIRCam imaging in the field from CEERS epoch 1 (2022 June), especially prioritizing targets with photometric redshifts of $z > 6$. Each target was observed using a "slitlet" aperture of three microshutters, and the design also included empty shutters for background subtraction. The shutter configuration for observations taken with the medium-resolution gratings and the prism are identical.

We performed an initial reduction of the NIRCam images in all four pointings, using version 1.5.3 of the JWST Calibration Pipeline (Bushouse et al. 2022)[40] with some custom modifications. We used the current (2022 July 15) set of NIRCam reference files,[41] though we note that the majority were created preflight, including the flats and photometric calibration references. We describe our reduction steps in greater detail in Finkelstein et al. (2022) and Bagley et al. (2023). Coadding the reduced observations into a single mosaic was performed using the drizzle algorithm with an inverse variance map weighting (Casertano et al. 2000; Fruchter & Hook 2002) via the Resample step in the pipeline. The output mosaics have pixel scales of $0\farcs03\ {\rm pixel^{-1}}$.

Photometry was computed on point-spread function (PSF) matched images using SExtractor (Bertin & Arnouts 1996) version 2.25.0 in two-image mode, with an inverse-variance-weighted combination of the PSF-matched F277W and F356W images as the detection image. Photometry was measured in all seven of the NIRCam bands observed by CEERS, as well as the F606W, F814W, F105W, F125W, F140W, and F160W HST bands using data obtained by the CANDELS and 3D-HST surveys (Grogin et al. 2011; Koekemoer et al. 2011; Brammer et al. 2012; Momcheva et al. 2016).

The CEERS NIRSpec observations (P. Arrabal Haro et al. 2023, in preparation) were reduced using version 1.8.5 of the JWST Science Calibration Pipeline (Bushouse et al. 2022) with the Calibration Reference Data System (CRDS) mapping 1027, starting from the Level 0 uncalibrated data products ("_uncal.fits" files) available on MAST. Custom parameters were used for the `jump` step at the detector-level calibration for a better treatment of the "snowballs"[42] produced by high-energy cosmic-ray events, and a nodded background subtraction was adopted.

The reduced 2D spectra ("s2d") have a rectified trace with a flat slope. The current version (1.8.5) of the pipeline does not correctly identify source locations in the 2D spectra for 1D spectra extraction. For the sources presented in this work, the 1D spectra were extracted using custom boxcar apertures centered on the visually identified continuum trace. Any remaining artifacts in the extracted spectra were masked after a detailed visual analysis. The flux uncertainties of the reduced 1D spectra appear to be underestimated by a factor of $\sim$2, as estimated from the normalized median absolute deviation (NMAD) of the flux in line-free regions, and so we rescale the flux uncertainty of each spectrum by a factor equal to the ratio of the line-free NMAD to the median pipeline uncertainty.

The current version (1.8.5) of the NIRSpec MSA data reduction uses a flux calibration that relies on preflight knowledge of the instrument, which is known to differ from the postlaunch performance (see Figure 20 of Rigby et al. 2023). The pipeline applies a correction for "slit losses" outside the MSA aperture using a *pathloss* reference file based on a prelaunch model for point sources that has not yet been fully verified on orbit. This correction may be inaccurate for extended sources or nondefault spectral extraction apertures; however, we find good agreement when comparing spectroscopic fluxes to our slit-extracted NIRCam photometry. Nonetheless, while any issues with absolute flux calibration may impact our interpretation of individual line fluxes or luminosities, the *relative* spectrophotometry of the reduced spectra is measured to be reliable, with line ratios of doublets ([O III] $\lambda\lambda$4960, 5008; Storey & Zeippen 2000) and Balmer lines (Osterbrock 1989) that match physical expectations

[40] http://jwst-pipeline.readthedocs.io/en/latest/

[41] http://jwst-crds.stsci.edu, http://jwst_nircam_0214.imap

[42] https://jwst-docs.stsci.edu/data-artifacts-and-features/snowballs-and-shower-artifacts

Table 1
AGN Sample

Source Name	R.A. (deg)	Decl. (deg)	z	$m_{\rm F356W}$ (mag)
CEERS 2782	214.823453	52.830281	5.242	25.8 ± 0.01
CEERS 746	214.809142	52.868484	5.624	26.9 ± 0.04

Note. CEERS 2782 is the same source as CEERS-AGN-z5-1 in O23.

(see additional discussion in Trump et al. 2023; P. Arrabal Haro et al. 2023, in preparation).

3. Sample Description

During the initial inspection of our reduced NIRSpec data, we identified two sources with broad Hα emission. Information on these sources, referred to as CEERS 2782 and CEERS 746, is listed in Table 1. CEERS 2782 was observed as a result of targeted follow-up of the AGN candidate CEERS-AGN-z5-1 identified by O23. CEERS 746 was selected for observation, as it was previously identified as a candidate massive galaxy at $z = 8.13$ by Labbe et al. (2023) and a potential strong-line emitter at $z = 5.72$ by Pérez-González et al. (2023). NIRCam images of both sources are shown in Figure 1, while their 1D and 2D spectra from the G395M grating are shown in Figure 2. Our derived redshifts, based on the [O III] $\lambda\lambda$4960, 5008 narrow lines, for CEERS 2782 and CEERS 746 are $z = 5.242$ and $z = 5.624$, respectively.

Based on surface brightness profile modeling using the `GALFIT` software (Peng et al. 2002), we find that the emission from both sources is best fit using a point-source model in all of the NIRCam bands in which they are detected. For this work we provided `GALFIT` with empirical PSFs constructed from the CEERS imaging and noise images that account for both the intrinsic image noise (e.g., background noise and readout noise) and added Poisson noise due to the objects themselves. We find that adding an additional single Sérsic model to a point-source model does not result in a considerable improvement in our flux residuals. As a result, we conclude that point-like emission dominates the light from both sources.

Neither CEERS 2782 nor CEERS 746 is directly detected in a variety of multiwavelength data sets that we inspected. This includes Very Large Array (VLA) 3 GHz observations (E. Jiménez-Andrade et al. 2023, in preparation; VLA programs 21B-292 and 22A-400; PI: M. Dickinson), SCUBA-2 850 μm submillimeter data (Zavala et al. 2017), and Chandra X-ray imaging from the AEGIS-XD survey (Nandra et al. 2015). Only CEERS 2782 falls within the CEERS MIRI observations, but it is not directly detected in the available F1500W imaging.

We estimate upper limits to the X-ray flux of both sources using the formalism from Kraft et al. (1991). Based on the observed counts in the 0.5–7 keV band at the location of each source, we find the 3σ single-sided upper limit on the full-band (0.5–10 keV) flux of CEERS 2782 and CEERS 746 to be 3.93×10^{-16} erg s^{-1} cm^{-2} and 4.96×10^{-16} erg s^{-1} cm^{-2}, respectively. This corresponds to rest-frame 0.5–10 keV X-ray luminosities below 3.81×10^{43} erg s^{-1} and 5.47×10^{43} erg s^{-1} at the redshifts of the two sources. Here the conversion from observed counts in the 0.5–7 keV band to flux in the standard 0.5–10 keV energy band was done assuming a power-law X-ray spectrum with a spectral index of $\Gamma = 1.4$ and Galactic $N_{\rm H}$ of 1.3×10^{20} cm^{-20} (Dickey & Lockman 1990).

In Figure 3, we show the NIRCam photometry and NIRSpec prism spectrum of both CEERS 2782 and CEERS 746. In the case of CEERS 2782, we find that the prism spectrum must be scaled by a factor of 2 to match the NIRCam broadband photometry. This may be due to potential slit losses, as CEERS 2782 sits near the edge of its microshutter slit, the outline of which can be seen in Figure 1. We find that no such correction is needed for the CEERS 746 prism spectrum.

As discussed by O23, the broadband photometry of CEERS 2782 is consistent with a single power-law function, with the exception of filters that are affected by strong-line emission, namely F277W, F410M, and F444W. A single power-law fit to the other four filters yields the best-fit power-law slope $\alpha_\lambda = -1.14 \pm 0.03$ ($\equiv d \ln F_\lambda / d \ln \lambda$), which is consistent with a typical value for unobscured quasars (e.g., Fan et al. 2001; Vanden Berk et al. 2001). This power-law model yields the absolute magnitude at rest-frame 1450 Å of $M_{1450} = -19.44 \pm 0.05$ mag. Likewise, the monochromatic luminosity at rest-frame 3000 and 5100 Å is $L_{3000} = (4.83 \pm 0.09) \times 10^{43}$ erg s^{-1} and $L_{5100} = (4.48 \pm 0.08) \times 10^{43}$ erg s^{-1}, respectively. We find that a low-redshift composite spectrum of quasars (the blue model in Figure 3 of Vanden Berk et al. 2001a, hereafter VB01) scaled to match the photometry can explain the observed spectral shape of CEERS 2782 well.

The SED of CEERS 746 shows more complexity. The source has a blue continuum spectrum with a UV slope of $\alpha_\lambda = -3.0 \pm 0.3$ at $\lambda_{\rm obs} \simeq 1$–2 μm and a very steep continuum spectrum ($\alpha_\lambda = 1.8 \pm 0.2$) with strong Balmer and [O III] emission lines at longer wavelengths. This steep spectral slope, coupled with the broad Hα emission we detect, suggests that this source is a heavily obscured, broad-line AGN (e.g., Gregg et al. 2002). In Figure 3(b), we overlay the composite SED of low-redshift broad-line AGNs (VB01) reddened assuming a color excess of $E(B-V) = 0.9$ and the extinction law discussed in Calzetti et al. (2000). Note that this model, shown with the cyan curve, is essentially the same as the QSO2 SED template provided in Polletta et al. (2006). This model traces the observed prism continuum at $\lambda_{\rm obs} \gtrsim 3$ μm well; however, the obscured broad-line AGN model does not explain the blue side of the observed spectrum, requiring additional components at these shorter wavelengths. We discuss more complex SED models, including fits using hybrid galaxy plus AGN models, in Section 6.3.

It should be noted that broad emission lines similar to those detected in CEERS 2782 and CEERS 746 can be produced by non-AGN-related mechanisms, such as starburst-driven galactic winds. However, if the broad velocity widths that we observe are the result of large-scale outflows, we would expect this broadened emission to be apparent in other emission lines in addition to Hα (e.g., Amorín et al. 2012; Hogarth et al. 2020). As discussed in Section 5.1, we do not observe any broad features in other lines detected with similarly high signal-to-noise ratio, such as the [O III] λ5008 emission line. Instead, [O III] and other forbidden lines have widths consistent with the narrow Hα component and inconsistent with the outflow scenario. Broad-line AGNs typically exhibit broad components for permitted lines (like Hα) and narrow widths of forbidden lines (like [O III]) (e.g., Vanden Berk et al. 2001; Schmidt et al. 2016), as observed in our spectra. This fact, coupled with the

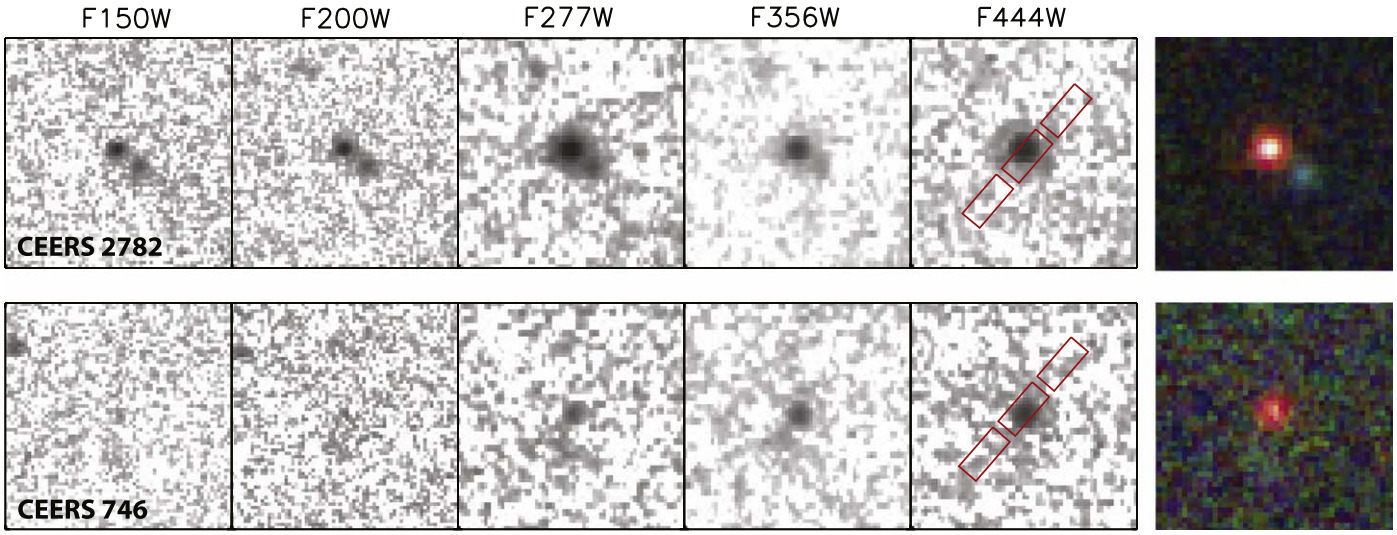

Figure 1. JWST NIRCam images of our broad-line AGN sample at $z > 5$ taken in the short-wavelength (F150W and F200W) and long-wavelength (F277W, F356W, and F444W) filters. The RGB images are composed of images in the F150W, F277W, and F444W filters. All images are $2'' \times 2''$ in size. The alignment of the NIRSpec microshutter aperture relative to each source is shown in red overlaying the F444W image.

shape of their SEDs, suggests that both CEERS 2782 and CEERS 746 host a low-luminosity AGN.

4. Line-fitting Analysis

The NIRSpec spectra of CEERS 2782 and CEERS 746 include several prominent emission lines. The G395M/F290LP spectrum of both sources includes strong Hα, Hβ, and [O III] $\lambda\lambda$4960, 5008 emission, and CEERS 746 also features a He I λ5877.25 line. Both sources exhibit a weak line near the expected wavelength of the [Fe X] λ6376 coronal emission line. The G235M/F170LP spectrum of both sources includes the [Ne III] λ3870.86 line, while CEERS 746 also exhibits the Hγ λ4341.69 and auroral [O III] λ4364.44 lines.

We measure line fluxes and uncertainties with a Levenberg–Marquardt least-squares method implemented by the `mpfit` IDL code (Markwardt 2009).[43] We fit isolated lines with single Gaussians and simultaneously fit multiple Gaussians for features in the Balmer line regions. The results of our line fits are shown in Figure 4.

To account for potential broad components, we fit the Hα line with two Gaussians: one narrow with width $\sigma < 350$ km s^{-1}, and one broad with width $\sigma > 350$ km s^{-1}. We also attempted to include additional Gaussian components for the [N II] $\lambda\lambda$6550, 6585 doublet. While the Hα and [N II] λ6585 lines are separated by roughly three times the resolution limit, the lines will blend together in the presence of a sufficiently broad Hα component. We account for this by constraining the line widths and relative line centers of the [N II] doublet to that of narrow Hα, but we find that the [N II] lines are not significantly ($>3\sigma$) detected and their inclusion does not improve the χ_0^2 of the fit. We report the 1σ upper limit for [N II] λ6585 but do not include it in the fits for broad and narrow Hα.

We also performed a simultaneous fit of the Hβ emission-line region with components for narrow Hβ and the [O III] $\lambda\lambda$4960, 5008 doublet. In both systems we tested a fit that included an additional broad ($\sigma > 350$ km s^{-1}) Hβ component but found that this component is only marginally ($<1\sigma$) detected and including it increases the χ_0^2 of the fit. We report 1σ upper limits for putative broad Hβ emission that assume the same width as the broad Hα component applied to the local noise of the Hβ region.

Finally, we fit single narrow Gaussians for the [O II] λ3728.48 (the 3727+3729 doublet is blended in the $R \simeq 1000$ medium-resolution NIRSpec grating), [Ne III] λ3870.86, Hγ λ4341.69, and [O III] λ4364.44 lines. The [Ne III] line is significantly ($>3\sigma$) detected in CEERS 2782, and all the other lines are only marginally ($<3\sigma$) detected.

5. Results

5.1. Emission-line Properties

Our two AGNs are identified from their broad Hα emission. As described above, we use a two-component fit with both narrow and broad Gaussian components in which the line centers, widths, and fluxes are free parameters. These broad +narrow fits have significantly lower χ_0^2 than single-Gaussian fits for the Hα lines. Both objects have best-fit narrow Hα components that are unresolved in the $R \sim 1000$ NIRSpec spectra, with narrow Hα widths of $\sigma = 135 \pm 9$ km s^{-1} and $\sigma = 131 \pm 24$ km s^{-1} for CEERS 2782 and CEERS 746, respectively. The best-fit broad Hα components have $\sigma = 840 \pm 120$ km s^{-1} and FWHM $= 2060 \pm 290$ km s^{-1} for CEERS 2782 and $\sigma = 720 \pm 87$ km s^{-1} and FWHM $= 1800 \pm 200$ km s^{-1} for CEERS 746 (fitting σ and FWHM independently). A summary of our line measurements is provided in Table 2.

In contrast, the Hβ emission lines of both objects are best fit by single narrow Gaussians, with no statistical improvement from including a broad component. Both Hβ lines appear to be unresolved, with best-fit single-Gaussian widths of $\sigma = 145 \pm 17$ km s^{-1} for CEERS 2782 and $\sigma = 108 \pm 33$ km s^{-1} for CEERS 746. We compute upper limits for a potential (undetected) broad Hβ component by assuming a Gaussian of the same width as the measured Hα broad lines with the noise properties of the Hβ region in the spectrum. In both cases the upper limit for potential Hβ broad emission is statistically consistent with a broad Hα/Hβ = 3.1 (Osterbrock 1989): CEERS 2782 has a lower limit

[43] https://pages.physics.wisc.edu/~craigm/idl/fitting.html

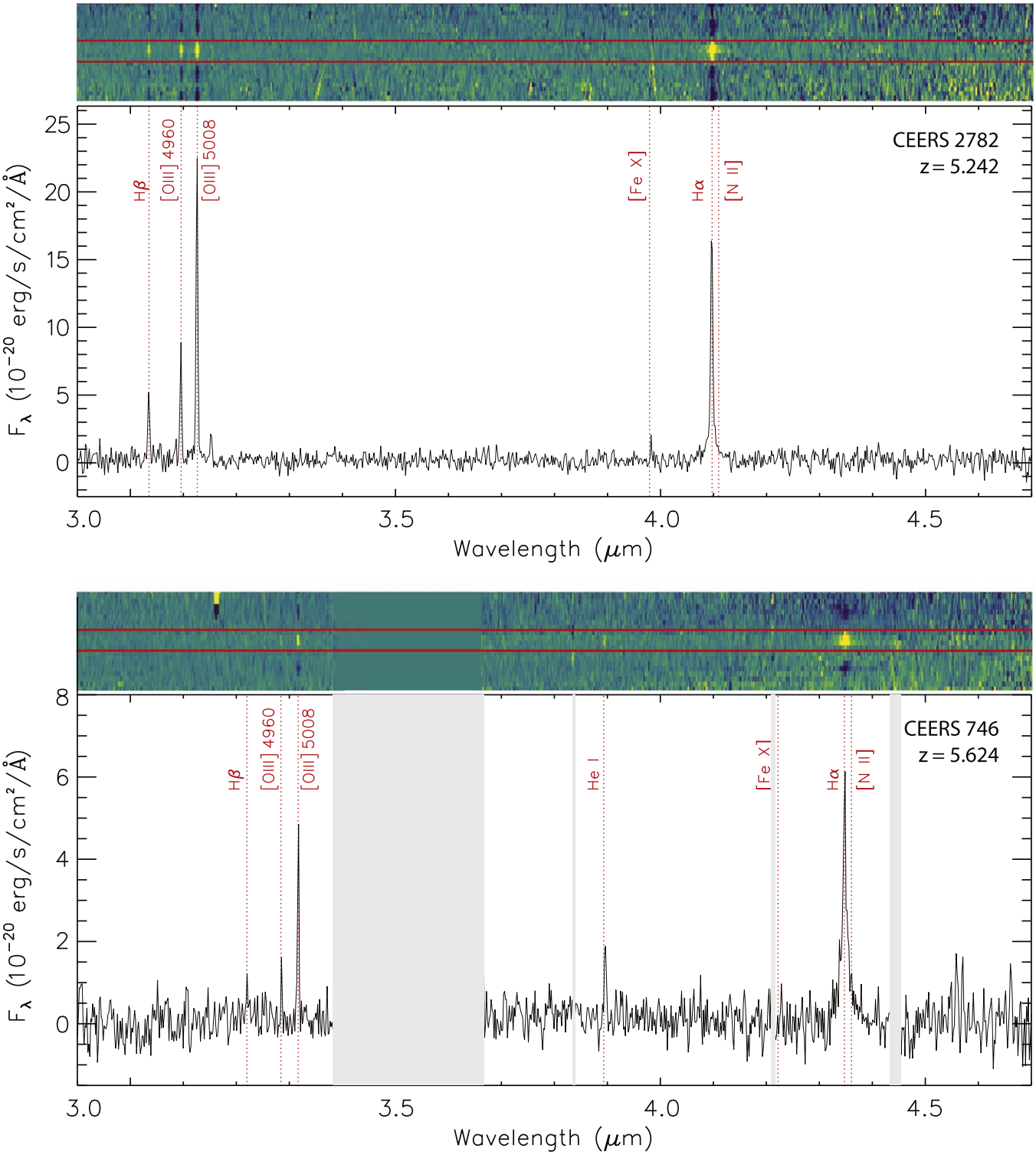

Figure 2. NIRSpec spectra of sources CEERS 2782 and CEERS 746 taken in the G395M grating with $R \sim 1000$. The 2D spectra are shown above with extraction windows highlighted in red. Gray regions in both the 1D and 2D spectra indicate regions masked owing to artifacts identified via visual inspection and the detector chip gap. The locations of several prominent emission lines are noted.

of broad Hα/H$\beta > 2.4$ (3σ), and CEERS 746 has a lower limit of Hα/H$\beta > 3.0$ (3σ). That is, the observed spectra of both objects are consistent (within $<3\sigma$) with being type 1 AGNs that have undetected broad Hβ lines that match the expectation for the intrinsic (unobscured) Balmer line ratios. Since both spectra have only upper limits for a broad Hβ component, the objects are also consistent with being type 1 AGNs with nonzero nebular attenuation affecting the broad lines, or with being type 1.5 AGNs with weaker broad Hβ emission. Definitively classifying the sources as unobscured type 1, obscured type 1, or type 1.5 AGNs would require spectra of higher signal-to-noise ratio (S/N).

The narrow Balmer emission lines imply modest dust attenuation in both objects. CEERS 2782 has a measured

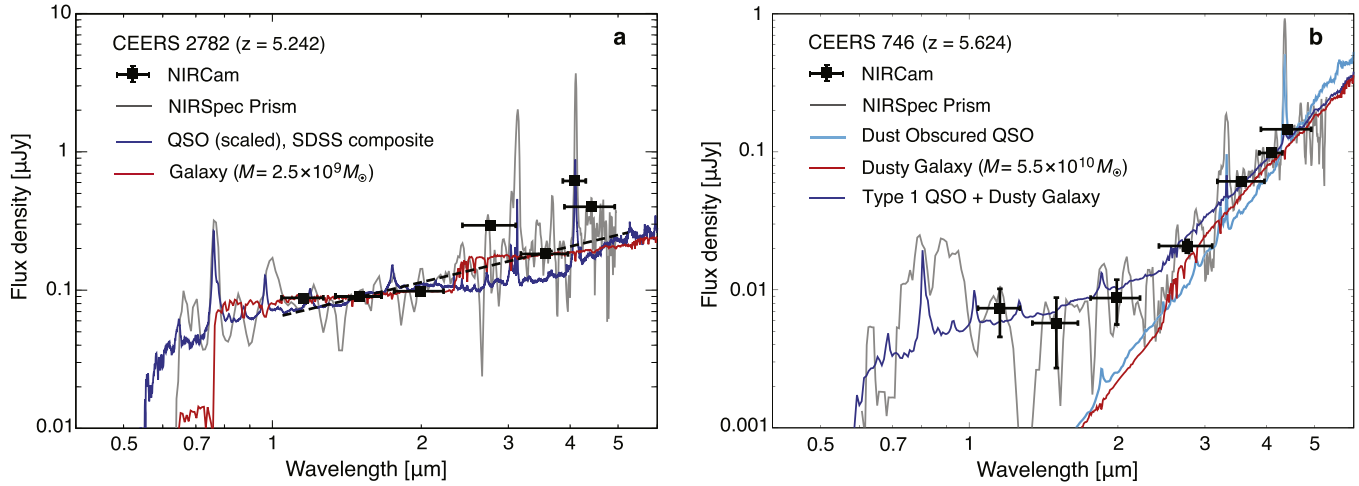

Figure 3. The SEDs of the two low-luminosity AGNs (CEERS 2782 and CEERS 746) obtained with the JSWT NIRSpec and NIRCam. (a) The continuum spectral shape is explained by the composite quasar spectrum of VB01 scaled to match the photometry of CEERS 2782 (blue) and is fitted well with a single power law with an index of $\alpha_\lambda = -1.14$ (dashed). The galaxy SED model with $M_\star \simeq 2.5 \times 10^9\, M_\odot$ is overlaid (red), where the stellar continuum in the F356W filter becomes comparable to the observed F356W flux density. This gives a robust upper bound of the underlying stellar population. (b) The source has a blue continuum spectrum with a UV slope of $\alpha_\lambda < -3.0$ at $\lambda_{\rm obs} \simeq 1$–$2\ \mu$m and a very steep continuum spectrum ($\alpha_\lambda \simeq 2.0$). The redder part can be explained by either a heavily obscured quasar (cyan) or a dusty starburst galaxy (red). As a possible explanation of the blue excess in the spectrum, the unobscured broad-line AGN contribution is added to the dusty starburst galaxy (blue). In the dusty galaxy model, the stellar mass is found to be $M_\star \simeq 5.5 \times 10^{10}\, M_\odot$ (see the text in Section 6.3).

narrow-line Balmer decrement of $H\alpha/H\beta = 3.9 \pm 0.5$, and CEERS 2782 has a narrow-line $H\alpha/H\beta = 5.3 \pm 2.1$. We use these Balmer decrements as priors to inform the SED fitting in Sections 6.2 and 6.3.

Intriguingly, both AGNs have weak emission-line features that are consistent with marginally detected [Fe X] λ6376, as seen in Figures 2 and 4. [Fe X] is a coronal emission line with an ionization potential of 262 eV that is observed in low-mass AGNs in the local Universe (e.g., Molina et al. 2021). The putative [Fe X] emission lines are marginally detected with S/N = 2.4 for CEERS 2782 and only S/N = 1.5 for CEERS 746. Both lines are best fit to be slightly redder than the other narrow-line features: if the marginal detections represent genuine emission lines, then they may indicate a kinematic offset between the extreme-ionization coronal gas and the narrow-line region.

Finally, in Figure 5 we plot the narrow emission line ratios of both sources on the BPT ([O III]/Hβ vs. [N II]/Hα; Baldwin et al. 1981) and OHNO ([O III]/Hβ vs. [Ne III]/[O II]; Backhaus et al. 2022) line ratio diagnostics that are commonly used to classify galaxies as dominated by emission from AGNs or star formation. The colored curves in Figure 5 indicate MAPPINGS V photoionization models from Kewley et al. (2019), with different colored curves for different ionizations ($\log(Q/[\mathrm{cm\ s^{-1}}]) = [7, 8, 9]$ increasing left to right), metallicity along each curve ($Z/Z_\odot = [1, 0.4, 0.2, 0.05]$ as indicated in the legend), and curves shown for each of three thermal pressures ($\log(Pk_{\rm B}^{-1}/[\mathrm{K\ cm^{-3}}]) = [7, 8, 9]$). The MAPPINGS V models use α-enhanced abundances as described in Nicholls et al. (2017), such that low metallicities include enhanced relative abundances of O and Ne (and a lower relative abundance of N). Figure 5 also includes comparison samples of high-redshift galaxy line ratios from early JWST spectroscopy: stacked CEERS measurements from Sanders et al. (2023) in the BPT and SMACS ERO galaxies from Trump et al. (2023) in the OHNO diagram.

At low redshift ($z \lesssim 2$), AGNs typically have higher [N II]/Hα, [O III]/Hβ, and [Ne III]/[O II] ratios owing to harder ionizing radiation from the AGN accretion disk, and line-ratio diagnostics shown in Figure 5 can be used to separate AGNs from star-forming galaxies. However, high-redshift galaxies show systematic offsets relative to galaxies and AGNs at $z = 0$, with higher ionization and lower metallicity in both AGNs and from star-forming H II regions (Shapley et al. 2005; Erb et al. 2006; Liu et al. 2008; Kewley et al. 2013a, 2013b; Sanders et al. 2023). Both CEERS 2782 and CEERS 746 have high [O III]/Hβ, low [N II]/Hα, and high [Ne III]/[O II] line ratios that are consistent with MAPPINGS V photoionization models for high ionization ($\log(Q/[\mathrm{cm\ s^{-1}}]) \simeq 8$) and moderately low metallicity ($Z/Z_\odot \simeq 0.2$–0.4).

The AGN line ratios and interstellar medium conditions implied in Figure 5 are virtually indistinguishable from star-forming galaxies observed at similar redshifts, since high-redshift H II regions have similarly high ionization and low metallicity to these $z \sim 5$ AGN narrow-line regions. Photoionization models show that low-metallicity AGNs can have similar [O III]/Hβ and [N II]/Hα ratios and lie within or even below the star-forming branch (Groves et al. 2006; Feltre et al. 2016). Although low-metallicity AGNs are rare in the local Universe (e.g., Storchi-Bergmann et al. 1998; Groves et al. 2006), recent simulations that make use of the AGN photoionization models presented in Feltre et al. (2016) predict that high-redshift, low-metallicity AGNs should primarily occupy the top portion of the local star-forming branch (Hirschmann et al. 2019, 2022), which is consistent with our findings. The fact that neither source is X-ray detected and that their BPT line ratios are similar to that of star-forming galaxies observed at the same redshift means that their broad-line emission may be one of the few ways to detect these high-redshift low-luminosity AGNs. Other possible approaches include diagnostics with high-ionization and extreme-ionization lines (e.g., He II and [Ne V]; Feltre et al. 2016; Nakajima & Maiolino 2022; Cleri et al. 2023). Preselection with photometric colors may also be useful to select fast-growing BHs with $M_{\rm BH} \sim 10^6$–$10^7\, M_\odot$ in metal-poor environments (Inayoshi et al. 2022b).

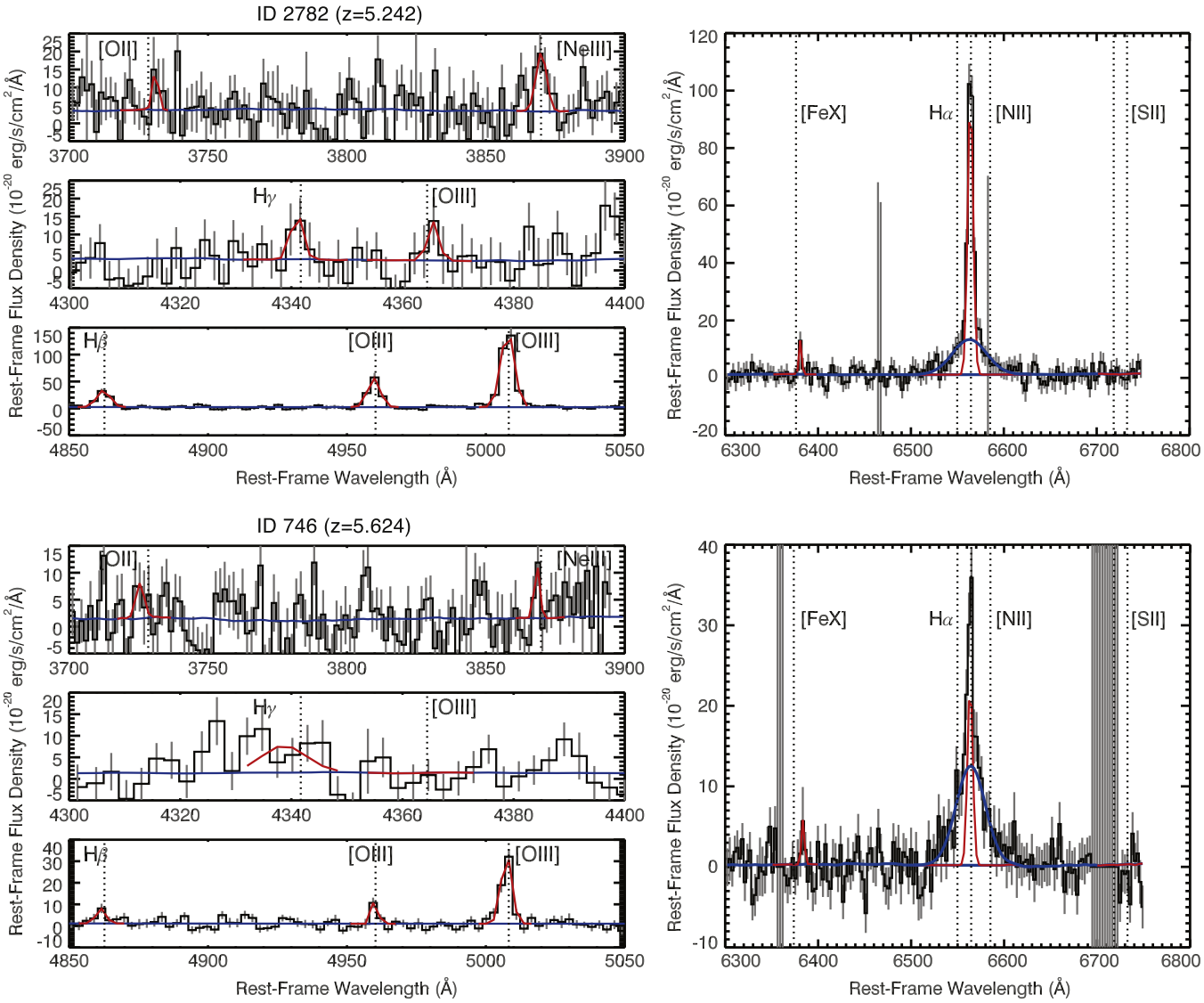

Figure 4. The rest-frame spectra (black histograms) and associated uncertainty (gray error bars) of both sources in regions with emission-line features. Red lines show the best-fit Gaussians for narrow emission lines, and the blue line shows the best-fit broad component for Hα, which have an FWHM of 2060 ± 286 km s^{-1} and 1802 ± 204 km s^{-1} for CEERS 2782 and CEERS 746, respectively.

5.2. Virial BH Mass Estimates

In this section, we estimate the virial BH masses of the two broad-line AGNs assuming that their broad Hα emission traces the kinematics of gas in the broad-line region. The single-epoch BH mass estimation method is best calibrated against the width of the broad Hβ emission line and the rest-frame 5100 Å continuum luminosity (L_{5100}) using the reverberation mapping technique (e.g., Kaspi et al. 2000). However, since we do not detect a broad Hβ component in our spectra, we instead employ the BH mass relationship proposed by Greene & Ho (2005, hereafter GH05), which relies entirely on Hα emission. This method has been widely used in, for example, BH mass estimates for AGNs in dwarf galaxies (e.g., Reines et al. 2013; Baldassare et al. 2015). This recipe is based on empirical correlations between Balmer emission-line luminosities and L_{5100} and between the line widths of Hβ and Hα.

In terms of the broad Hα line width and L_{5100}, the BH mass formula is expressed as

$$M_{\rm BH} = 5.04 \times 10^6\, M_\odot \left(\frac{L_{5100}}{10^{44}\ {\rm erg\ s^{-1}}}\right)^{0.64} \left(\frac{{\rm FWHM_{H\alpha}}}{10^3\ {\rm km\ s^{-1}}}\right)^{2.06}. \quad (1)$$

This equation is based on the formula of Kaspi et al. (2000) for Hβ with the Hβ line width substituted with that of Hα (Equation (3) of GH05). It is important to note that this equation assumes that the 5100 Å continuum luminosity is dominated by light from the AGN. Alternatively, we can directly apply the virial BH mass recipe of GH05, which is based on the broad Hα line width and luminosity:

$$M_{\rm BH} = 2.0 \times 10^6 \left(\frac{L_{\rm H\alpha}}{10^{42}\ {\rm erg\ s^{-1}}}\right)^{0.55} \left(\frac{{\rm FWHM_{H\alpha}}}{10^3\ {\rm km\ s^{-1}}}\right)^{2.06} M_\odot. \quad (2)$$

First, we use the line width of the broad Hα component detected in our NIRSpec spectroscopy, corrected for the

Table 2
Derived AGN Properties

ID	M_{1450} (mag)	L_{5100} (10^{43} erg s^{-1})	$L_{H\alpha}$(broad) (10^{42} erg s^{-1})	FWHM$_{H\alpha,broad}$ (km s^{-1})	M_{BH} ($10^7\,M_\odot$)	λ_{Edd}	$M_\star$ ($10^9\,M_\odot$)	(Hα/Hβ)$_{obs}$
2782	-19.4 ± 0.05	4.48 ± 0.08	1.64 ± 0.21	2060 ± 290	1.3 ± 0.4	0.15 ± 0.04	<2.5	3.9 ± 0.5
746	See text		1.67 ± 0.16	1800 ± 200	0.90 ± 0.22	0.29 ± 0.08	<55.0	5.3 ± 2.1
$746_{A_v=4}$	See text		34.4 ± 3.4	1800 ± 200	4.7 ± 1.2	3.5 ± 0.9	<55.0	5.3 ± 2.1

Note. The BH mass for CEERS 2782 uses L_{5100} estimated from the photometric SED and the line width of broad Hα (FWHM$_{H\alpha,broad}$) (Equation (1)), while for CEERS 746 we use FWHM$_{H\alpha,broad}$ and line luminosity of broad Hα (Equation (2)). The bolometric luminosity is also converted from $L_{H\alpha}$ for CEERS 746. In the third row, we show the case when CEERS 746 is heavily dust reddened with $A_V = 4$.

$R \sim 1000$ instrumental resolution, and L_{5100} derived from the photometric SEDs to estimate the virial BH masses of CEERS 2782. Using Equation (1) results in a BH mass of $M_{BH} = (1.3 \pm 0.4) \times 10^7\,M_\odot$, with the Eddington ratio of $L_{bol}/L_{Edd} = 0.15 \pm 0.04$. We use the bolometric luminosity inferred from L_{3000} to be consistent with other $z > 5$ BH mass estimates in the literature. We apply a bolometric correction of $L_{bol} = 5.15 L_{3000}$ (Richards et al. 2006) to derive $L_{bol} = (2.49 \pm 0.04) \times 10^{44}$ erg s^{-1}. Using instead the Hα line width and luminosity, Equation (2) yields $M_{BH} = (1.1 \pm 0.3) \times 10^7\,M_\odot$. This value is more systematically uncertain than our first estimate, although consistent within the 1σ error, due to potential slit losses (see Section 2).

The BH mass estimate for CEERS 746 is complicated because of its potentially obscured nature. Taking the observed Hα luminosity at face value and applying Equation (2), we derive a mass of $M_{BH} = (9.0 \pm 2.2) \times 10^6\,M_\odot$. We caution that this value is likely a lower limit since the Hα emission is likely affected by dust extinction. If we assume that a dust-reddened AGN continuum dominates the observed rest-optical spectrum with $A_V = 4$ (see Section 6.3), the inferred BH mass could be as high as $M_{BH} = (4.7 \pm 1.2) \times 10^7\,M_\odot$. A careful decomposition of the AGN/host components and, if the AGN is dust reddened, measurements of AGN continuum luminosity at rest-frame infrared wavelengths (Greene et al. 2014; Kim et al. 2015) are required to better estimate the intrinsic continuum luminosity and subsequently the virial mass for this AGN.

6. Discussion

6.1. The M_{BH}–L_{bol} Distribution

The successful spectroscopic identification of two low-luminosity broad-line AGNs at $z > 5$ opens up a new parameter space for high-redshift AGN studies, thanks to the unprecedented infrared sensitivity of JWST and the multiwavelength photometric data set available in the EGS field. Figure 6 shows the distribution of $z \gtrsim 5$ AGNs in the BH mass–bolometric luminosity plane with the two new low-luminosity AGNs shown in red and orange. A summary of the measured properties of these two AGN is provided in Table 2.

As is discussed in O23, CEERS 2782 is 2–3 dex fainter than known quasars at $z \gtrsim 5$ (e.g., Willott et al. 2010; Trakhtenbrot et al. 2011; Matsuoka et al. 2019; Onoue et al. 2019; Shen et al. 2019; Kato et al. 2020) and more comparable to those of typical nearby AGNs (e.g., Liu et al. 2019). The virial BH mass estimate we present above now shows that this low-luminosity AGN is by far the least massive BH known in the Universe at the end of cosmic reionization. The modest Eddington ratio of CEERS 2782 suggests that this AGN has been identified after its rapid accretion mode has ended, although it is possible that the system will experience future bursts of heavy accretion (Li et al. 2023).

For CEERS 746, if we use the observed Hα luminosity without an extinction correction, then the BH powering this AGN may have a relatively low mass, comparable to the one detected in CEERS 2782. CEERS 2782. However, if we assume heavy dust attenuation ($A_V = 4$), it becomes a BH accreting at a rate above the Eddington limit. In Figure 6, we show our results assuming both no extinction for the Hα luminosity and $A_V = 4$ with the bolometric luminosity converted from L_{5100} estimated from the Hα luminosity. Adopting a more moderate level of dust extinction inferred from the observed Balmer decrement in the NIRSpec spectrum (Hα/H$\beta = 5.3$; $A_V = 1.9$) brings the bolometric luminosity of the source closer to the Eddington value. Thus, CEERS 746 is likely in its most active mode of accretion and on the way to expelling the material that currently obscures it. Fujimoto et al. (2022) report a dust-reddened AGN at $z = 7.19$, the BH mass of which is estimated to be $M_{BH} \lesssim 10^8\,M_\odot$ based on the upper limit of its X-ray luminosity. Although not confirmed, their AGN and CEERS 746 may be drawn from the same population of high-redshift dust-reddened AGNs. We discuss this scenario in greater detail in Section 6.3.

It is worth noting that the bolometric corrections and BH mass relationships that we employ were calibrated on local type 1 quasars. It remains to be determined how well these relationships hold (and with what scatter) for low-luminosity, broad-line AGNs at higher redshifts. Therefore, the errors we report for our bolometric luminosities and BH masses do not encompass any systematic error that may result from this.

6.2. Constraints on the Host Galaxy Mass of CEERS 2782

Figure 3(a) shows the prism spectrum and NIRCam photometric flux densities of CEERS 2782. As discussed in Section 3, the continuum spectral shape can be explained by the low-redshift composite quasar spectrum of VB01. Since the observed spectrum is dominated by the central AGN contribution, it is challenging to estimate the stellar mass of the host galaxy. Following the approach of Kocevski et al. (2023), we perform a two-component SED fit using `FAST` v1.1 (Kriek et al. 2009; Aird et al. 2018), which allows for simultaneous fitting of both galaxy and AGN models/templates. For this fit, we assume a Chabrier (2003) initial mass function, Bruzual & Charlot (2003) stellar population models, fixed solar metallicity, Calzetti et al. (2000) dust attenuation, and a "delayed-τ" star formation history with τ in the range of 0.1 Gyr to the age of the Universe at the source redshift (e.g., Maraston et al. 2010). We supplement these models with a library of nine empirically determined AGN templates. These include the composite quasar spectrum of VB01, five AGN-dominated

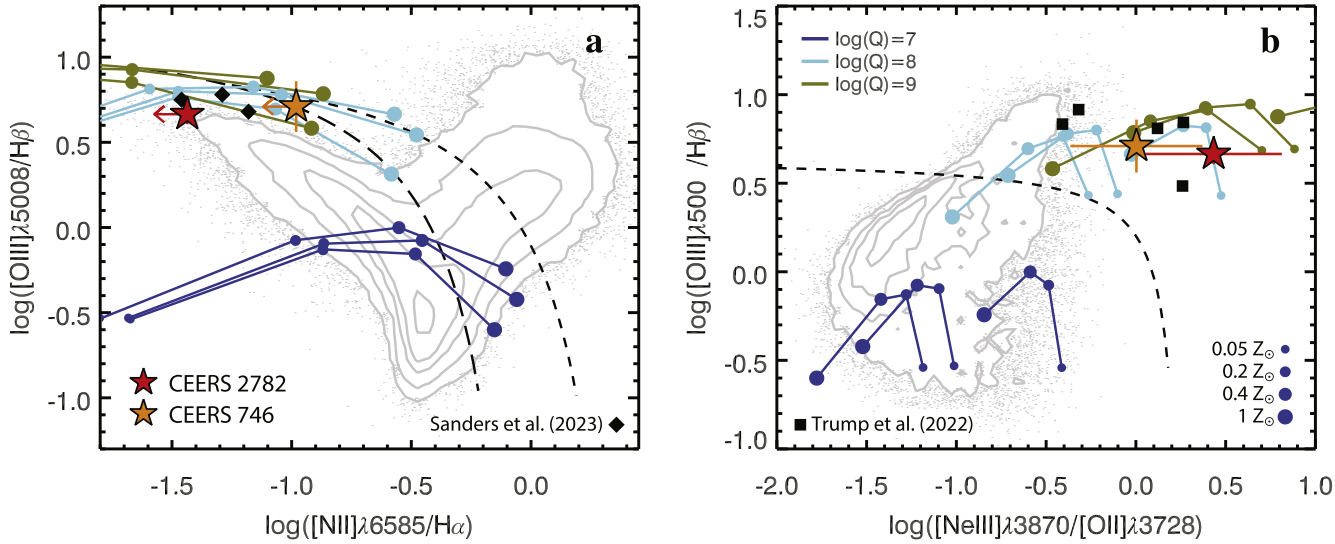

Figure 5. (a) The BPT emission-line diagnostic diagram. The gray contours denote the distribution of local star-forming galaxies and AGNs as measured by the SDSS (York et al. 2000). Black diamonds denote stacked line ratios of CEERS galaxies at $z \sim 5.6$, $z \sim 4.5$, and $z \sim 3.3$ (Sanders et al. 2023). The black- long and short-dashed lines denote the $z = 0$ and $z = 2.3$ boundary between the star-forming and AGN regions of the diagram defined by Kauffmann et al. (2003) and Kewley et al. (2013b), respectively. (b) The OHNO diagnostic diagram. Black squares denote line ratios of SMACS ERO galaxies at $5.3 < z < 8.5$ (Trump et al. 2023), and gray contours denote the distribution of $z \sim 0$ SDSS galaxies. The dashed line denotes the boundary between star-forming and AGN regions as defined in Backhaus et al. (2022). Colored curves in both panels show MAPPINGS V photoionization models (Kewley et al. 2019). The three color-coded sets of curves and points along those curves correspond to different ionization parameters and metallicities, as indicated by the legends, with three curves for each color corresponding to different gas pressures as described in the text. Both of our $z \sim 5$ AGNs have narrow-line ratios that are consistent with low metallicity and high ionization, with little difference from the emission-line ratios observed for other populations of high-redshift galaxies.

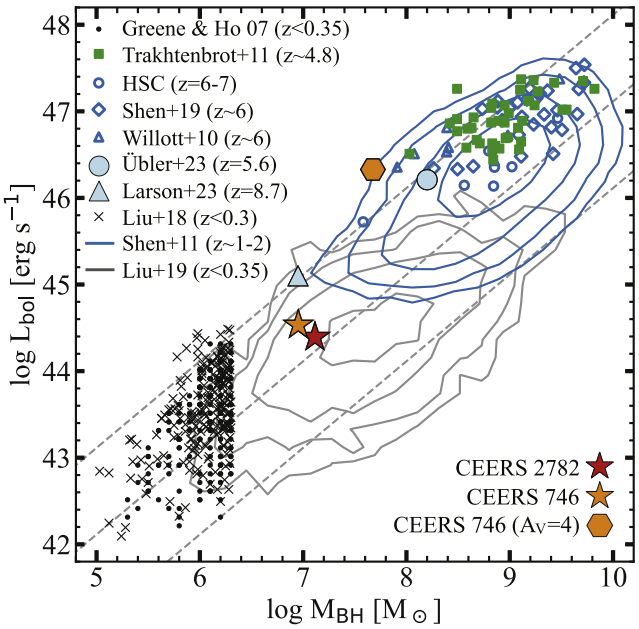

Figure 6. The BH mass–bolometric luminosity plane. Quasar samples at $z \geqslant 5$ are shown as blue and green symbols and contours, while low-redshift AGNs are shown in black. CEERS 2782 and CEERS 746 have BH masses 1–2 dex below those of known high-redshift quasars and more comparable to those of typical nearby AGNs. Two $z > 5$ AGNs recently discovered by JWST are also shown for comparison (light blue; Larson et al. 2023; Übler et al. 2023). See Section 6.1 for details on the uncertainties of these measurements.

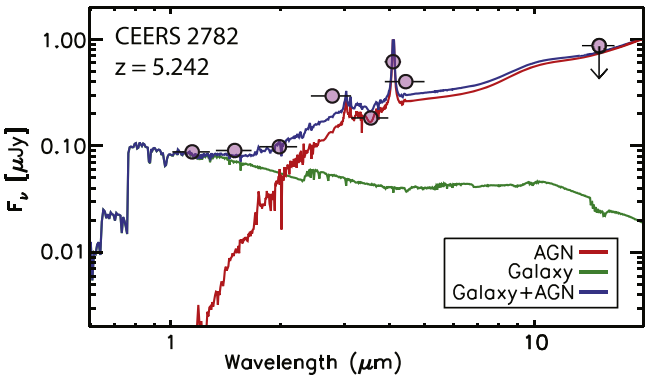

Figure 7. Multicomponent SED fit for CEERS 2782 using a linear combination of galaxy and AGN templates. The galaxy and AGN contributions are shown in green and red, respectively, while their sum is shown in blue. The host mass implied by this fit is $M_* = 10^8\ M_\odot$.

templates from the Polletta et al. (2007) SWIRE template library (namely, the Torus, TQSO1, BQSO1, QSO1, and QSO2 templates), and three composite SEDs of X-ray-selected AGNs with absorption column densities of $N_{\rm H} = 10^{22}$–10^{23} cm^{-2}, 10^{23}–10^{24} cm^{-2}, and 10^{24-25} cm^{-2} from Silva et al. (2004). The SED fit was carried out using photometry in all seven of the NIRCam bands observed by CEERS, as well as a 3σ upper limit on the flux density at 15 μm based on the depth of the MIRI F1500W imaging estimated in G. Yang et al. (2023, in preparation).

The results of our multicomponent SED fit is shown in Figure 7. We find that CEERS 2782 is best fit by a linear combination of AGN emission at long wavelengths and galaxy light at short wavelengths, with an implied host mass of $M_* = 10^8\ M_\odot$. However, we caution that this model predicts that the host galaxy should dominate the emission from the source in the F150W and F200W bands, whereas the source appears point-like in all of the NIRCam imaging. Therefore, based on the morphology of the source, it is likely that nuclear light dominates the emission from CEERS 2782 at all wavelengths.

We can derive a more conservative upper bound on the host mass by assuming that all of the observed light is due to stellar

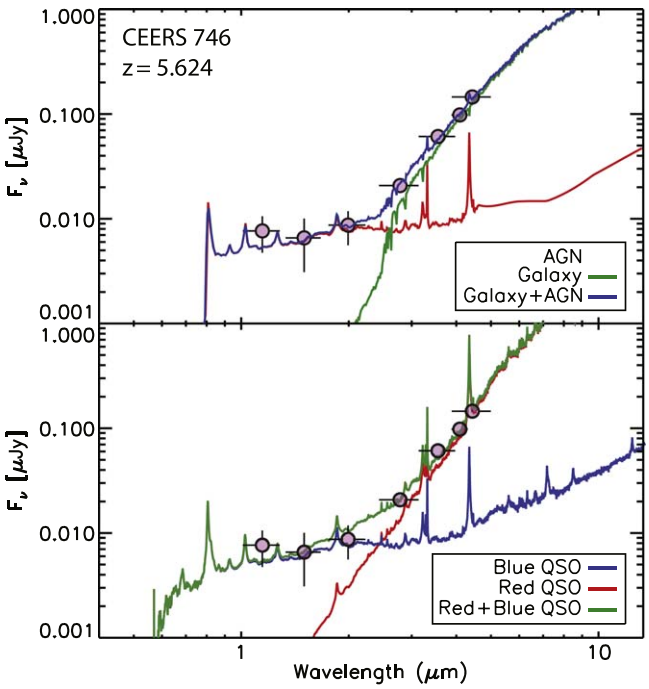

Figure 8. Multicomponent SED fits for CEERS 746. Top panel: best-fit linear combination of galaxy and AGN templates. The galaxy and AGN contributions are shown in green and red, respectively, while their sum is shown in blue. The host mass implied by this fit is $M_* = 5.5 \times 10^{10}\,M_\odot$. Bottom panel: an alternative SED fit assuming that nuclear light dominates the emission at all wavelengths and that the observed blue excess is due to scattered light from a patchy obscuring medium. The best-fit SED (green) is the linear combination of a heavily obscured quasar with $A_V = 4.0$ (red) and an unobscured quasar (blue). See Section 6.3 for details.

emission from the galaxy. For this purpose, we assume the galaxy model described above but fix the color excess of the stellar continuum to $E_s(B-V) = 0.09$, which is calculated from the Balmer decrement of the narrow emission lines we detect in the NIRSpec spectra (see Section 5.1). For this fit we exclude bands that are affected by strong-line emission, namely F277W, F410M, and F444W. The resulting fit returns a host mass of $M_\star = 2.5 \times 10^9\,M_\odot$. This galaxy SED model is shown in Figure 3(a) as the red curve. We note that this upper bound depends significantly on the low-mass end ($m_{\star,\rm min}$) of the stellar IMF; for instance, the upper bound is reduced by a factor of ~3 for $m_{\star,\rm min} = 1.0\,M_\odot$.

6.3. The Obscured Nature of CEERS 746

Figure 3(b) shows the prism spectrum and NIRCam photometric flux densities of CEERS 746. The red spectral shape with an index of $\alpha_\lambda \simeq 2.0$ at longer wavelengths can be explained either by a heavily obscured quasar (cyan) or a dusty starburst galaxy (red). Both models require the existence of obscuring material along the line of sight: a typical visual extinction of $A_V \simeq 3.65$ and 4.0 for the obscured quasar and dusty galaxy model, respectively. However, neither of the SED models explains the excess of the observed spectrum at $\lambda_{\rm obs} \lesssim 2\,\mu$m, requiring additional blue components.

The spectral shape of CEERS 746 could be explained by the combination of quasar emission at short wavelengths and light from a heavily obscured starburst galaxy dominating at long wavelengths. This combination of AGN plus galaxy light is shown as the blue curve in Figure 3(b) and in the top panel of Figure 8. If this is the case, CEERS 746 would be caught in a transition stage, moving from a dust-obscured starburst to an unobscured luminous quasar by expelling gas and dust. This model hypothesis is consistent with the dust-reddened AGN at $z = 7.19$ reported by Fujimoto et al. (2022), the BH mass of which is similar to that of CEERS 746. This would make CEERS 746 a dusty progenitor of the luminous, unobscured quasars observed by ground-based quasar surveys.

We can place a constraint on the host galaxy mass of CEERS 746 following the same arguments used for CEERS 2782. Our best-fit hybrid AGN plus galaxy model from FAST is shown in the top panel of Figure 8. The SED is best fit by a linear combination of a type 1 QSO template at short wavelengths and a heavily dust-obscured ($A_V \simeq 4.0$) galaxy at long wavelengths. The implied host mass is $5.5 \times 10^{10}\,M_\odot$. We note that the inferred host mass does not change significantly if we assume that all of the observed light from CEERS 746 is due to stellar emission from the galaxy because the steep spectral slope at $\lambda_{\rm obs} > 3\,\mu$m is dominated by the galaxy component in both the AGN+galaxy and galaxy-only scenarios.

An alternative explanation for the blue excess in the SED of CEERS 746 is dust (and electron) scattering, which preserves the spectral shape of the intrinsic broad-line AGN component (e.g., Zakamska et al. 2005). In the bottom panel of Figure 8, we show that the SED shape of CEERS 746 can be reproduced using a linear combination of a heavily reddened ($A_V = 4.0$) quasar spectrum from VB01 and an unreddened version of the same spectrum for the blue scattered component. Obscured quasars at low redshifts ($z < 2.5$) tend to show optical polarization levels higher than those of unobscured populations (Alexandroff et al. 2018). The fraction of the scattered flux relative to the primary component depends on the covering factor of the scattering medium and our viewing angle. For instance, assuming that 0.6% of the radiation flux of the intrinsic spectrum is scattered to our line of sight (see the Torus model in Polletta et al. 2006), the total SED is consistent with the photometric flux densities. We note that in this scenario nuclear light is predicted to dominate the emission from CEERS 746 at all wavelengths, which is consistent with the point-like morphology of the source.

Nevertheless, it is difficult to distinguish these two scenarios using the current data. Thus, multiwavelength follow-up observations such as rest-frame infrared and far-infrared imaging are needed to further constrain the nature of CEERS 746. We leave a more detailed SED analysis of this source to future work.

6.4. BH–Galaxy Coevolution at z ≃ 5

The empirical relation between the masses of SMBHs and their host galaxies is considered to be one of the most important outcomes of their mutual evolution over the cosmic timescale (e.g., Kormendy & Ho 2013). To constrain how and when the BH–galaxy correlations were established, the $M_\star$–$M_{\rm BH}$ distribution at the earliest epoch of the Universe needs to be unveiled. The apparent location of high-z quasars and their hosts also gives us more information on the BH growth mechanisms and their seeding processes (Hu et al. 2022; Inayoshi et al. 2022a; Scoggins et al. 2023).

Our first source, CEERS 2782, is a broad-line AGN with a BH mass of $M_{\rm BH} \simeq 1.3 \times 10^7\,M_\odot$ hosted in a star-forming galaxy with a stellar mass limited below $M_\star < 2.5 \times 10^9\,M_\odot$. Our second source, CEERS 746, is inferred to be a heavily

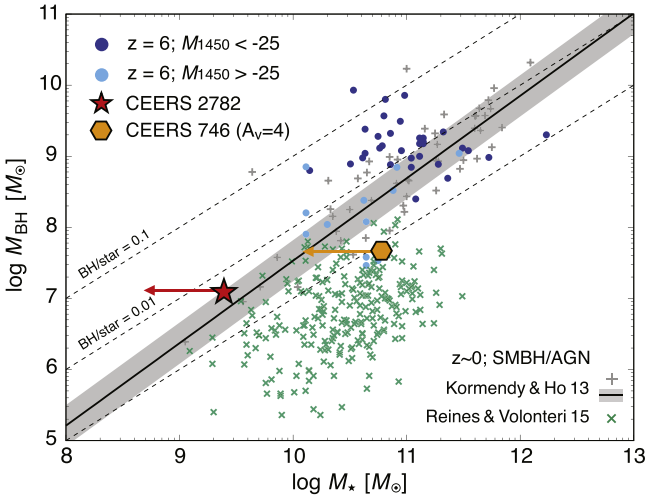

Figure 9. The BH mass vs. stellar mass relation of CEERS 2782 (red) and CEERS 746 (orange; $A_V = 4$). Circles show the $z > 6$ quasar samples compiled by Izumi et al. (2021): brighter ones with $M_{1450} < -25$ mag (blue), and fainter ones with $M_{1450} > -25$ mag (cyan). The gray and green crosses are the observational samples in the local Universe provided by Kormendy & Ho (2013) and Reines & Volonteri (2015), respectively. The diagonal dashed lines represent $M_{\rm BH}/M_\star = 0.1$, 0.01, and 10^{-3}.

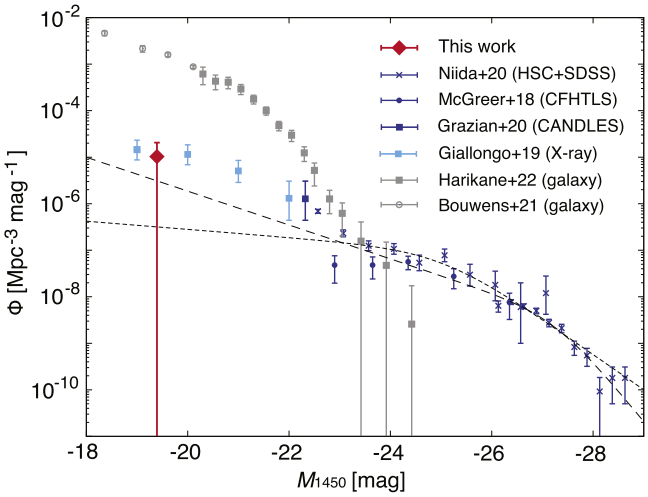

Figure 10. The AGN luminosity function at $z \sim 5$ based on CEERS 2782 (red) with the Poisson error from one object. The binned luminosity functions from the literature are shown for AGNs (McGreer et al. 2018; Giallongo et al. 2019; Grazian et al. 2020; Niida et al. 2020) and Lyman break galaxies (Bouwens et al. 2021; Harikane et al. 2022). The short-dashed line represents the parametric luminosity function of Niida et al. (2020), and the long-dashed line is from Finkelstein & Bagley (2022b) without a correction term from a double power-law function (i.e., $\delta = 0$ in their Equation (1)).

obscured broad-line AGN with a BH mass of $M_{\rm BH} \simeq 4.7 \times 10^7\, M_\odot$ (or $9.0 \times 10^6\, M_\odot$ unless it is obscured). The host stellar mass is possibly as high as $M_\star \lesssim 5.5 \times 10^{10}\, M_\odot$ in the case of the hybrid quasar + dusty galaxy model.

Figure 9 shows the $M_\star$–$M_{\rm BH}$ distribution of $z \gtrsim 6$ quasars compiled in Izumi et al. (2021; circle) for which the stellar mass is assumed to be the [C II]-based dynamical mass. CEERS 2782 is located in the lower left corner of the plane, which is uniquely separated from the $z \gtrsim 6$ quasar population already known (e.g., Wang et al. 2013; Venemans et al. 2016; Izumi et al. 2021). The mass ratio of $M_{\rm BH}/M_\star > 5.2 \times 10^{-3}$ for CEERS 2782 is consistent with or higher than that expected from the empirical relation seen in massive galaxies at $z = 0$ (black line; Kormendy & Ho 2013) but is overmassive compared to the BH-to-galaxy mass ratio measured for nearby broad-line AGNs whose virial BH masses are estimated to be as low as that of CEERS 2782 (Reines & Volonteri 2015). On the other hand, adopting the dust-corrected BH mass and dusty galaxy SED model, CEERS 746 is located well below the empirical relation at $z \simeq 0$. An important caveat is that the upper bound of the stellar mass can be reduced by a factor of $\simeq$3–5 with a different stellar population and star formation history (see discussion in Section 6.2). Further follow-up observations would give a better estimate of the stellar mass. The existence of such an overmassive BH, if confirmed, provides us with a unique opportunity to study the early stage of the BH–galaxy assembly.

6.5. Update of z ∼ 5 AGN Luminosity Function

We update the UV luminosity function of $z = 5$ AGNs from O23, based on the spectroscopic redshift of CEERS 2782. We do not include CEERS 746 in our discussion because of its unconstrained intrinsic UV luminosity. Following O23, we do not aim to provide statistical constraints on the luminosity function based on our small and incomplete sample; rather, we quantify the serendipity of our discovered low-luminosity AGNs at $z > 5$ in the 34.5 arcmin^2 of the first NIRCam pointings of the CEERS survey. Adopting the spectroscopic redshift of $z = 5.24$ and the redshift interval of $\Delta z \pm 0.5$, we derive the AGN number density of $\Phi = 1.07 \times 10^{-5}$ Mpc^{-3} mag^{-1} at the UV magnitude of $M_{1450} = -19.4$ mag. The difference from O23 ($\Phi = 1.03 \times 10^{-5}$ Mpc^{-3} mag^{-1}) is tiny because the central redshift of $z = 5.24$ has only slightly changed from the redshift used in their study ($z = 5.15$). The updated luminosity function is presented in Figure 10.

The faint end of the $z > 5$ AGN/quasar luminosity function is a matter of debate because low-luminosity AGNs produce more ionizing photons in a certain cosmic volume than do much rarer luminous AGNs, and thus its steepness is critical to infer the relative role in the cosmic reionization with respect to star-forming galaxies (e.g., Giallongo et al. 2015, 2019; Onoue et al. 2017; Matsuoka et al. 2018; McGreer et al. 2018; Finkelstein et al. 2019; Grazian et al. 2020, 2022; Kim et al. 2020; Niida et al. 2020; Kim & Im 2021; Yung et al. 2021; Finkelstein & Bagley 2022a; Jiang et al. 2022). The space density that we infer suggests that low-luminosity AGNs such as CEERS 2782 may in fact be common, in agreement with previous studies that have identified candidate faint quasars (e.g., Faisst et al. 2022; Fujimoto et al. 2022). However, a complete survey of low-luminosity AGNs with a well-defined selection function, as well as a careful analysis of host galaxy contribution to the UV magnitudes (Bowler et al. 2021; Adams et al. 2023; Harikane et al. 2022), is required to statistically argue the AGN abundance at the faint end, and subsequently the relative contribution of AGNs to the cosmic hydrogen/helium reionization.

7. Conclusions

We make use of JWST NIRSpec spectroscopy from the CEERS survey to identify two low-luminosity AGNs at $z > 5$ with broad Hα emission in their spectra. The first source, CEERS 2782 at $z = 5.242$, has a UV magnitude of $M_{1450} = -19.4 \pm 0.05$, making it 2–3 dex fainter than known quasars at similar redshifts. The source was previously identified as a candidate low-luminosity AGN based on

broadband photometry by O23. We measure an FWHM of 2038 ± 286 km s^{-1} for the broad Hα component, resulting in a BH mass of $M_{\rm BH} = (1.3 \pm 0.4) \times 10^7\, M_\odot$, making this the least massive BH known in the Universe at the end of cosmic reionization.

The second source, CEERS 746 at $z = 5.624$, has a blue continuum spectrum at short wavelengths ($\lambda_{\rm obs} < 3\,\mu$m) and a steep spectral slope at longer wavelengths. The SED shape suggests that this source is a broad-line AGN possibly caught in a transition phase between a dust-obscured starburst and an unobscured quasar. We measure an FWHM of 1807 ± 207 km s^{-1} for the broad Hα component, resulting in a BH mass in the range of $M_{\rm BH} \simeq (0.9\text{–}4.7) \times 10^7\, M_\odot$, depending on the level of dust obscuration assumed.

We derive upper limits on the host mass of each AGN and place constraints on the $M_\star$–$M_{\rm BH}$ relationship in the lowest mass range yet probed in the early Universe. We find that the host of CEERS 2782 is limited to $M_\star < 2.5 \times 10^9\, M_\odot$, while the host mass of CEERS 746 can be an order of magnitude larger ($5.5 \times 10^{10}\, M_\odot$) if we assume a visual extinction of $A_V = 4.0$, as inferred from our SED fitting. The $M_{\rm BH}/M_\star$ ratio for CEERS 2782, in particular, is consistent with or higher than the empirical relationship seen in massive galaxies at $z = 0$ but is overmassive compared to the BH-to-galaxy mass ratio measured for nearby broad-line AGNs whose virial BH masses are estimated to be as low as that of CEERS 2782.

We examine the narrow emission line ratios of both sources and find that their location on the BPT and OHNO diagrams is virtually indistinguishable from star-forming galaxies observed at similar redshifts, but also consistent with model predictions for moderately low metallicity AGNs with $Z/Z_\odot \simeq 0.2\text{–}0.4$. The fact that neither source is X-ray detected and their emission-line ratios in the BPT diagram are similar to those of star-forming galaxies means that their broad-line emission may be one of the few ways to detect these AGNs. Other possible approaches include diagnostics with high-ionization lines (e.g., He and Ne; Feltre et al. 2016; Nakajima & Maiolino 2022). Preselection with photometric colors may also be useful to select fast-growing BHs with $M_{\rm BH} \sim 10^6\text{–}10^7\, M_\odot$ in metal-poor environments (Inayoshi et al. 2022b).

The spectroscopic discovery of two low-luminosity, low-mass AGNs at $z > 5$ demonstrates the capabilities of JWST to push the BH mass limit closer to the range predicted for the BH seed population. Future work to uncover these low-luminosity AGNs, which are the dominant BH population at high redshift, will be the key to further constraining their abundance and the early growth history of SMBHs and their host galaxies.

Acknowledgments

This work is supported by NASA grants JWST-ERS-01345 and JWST-AR-02446 and based on observations made with the NASA/ESA/CSA James Webb Space Telescope. The data were obtained from the Mikulski Archive for Space Telescopes at the Space Telescope Science Institute, which is operated by the Association of Universities for Research in Astronomy, Inc., under NASA contract NAS 5-03127 for JWST. The specific observations analyzed can be accessed via doi: 10.17909/z7p0-8481. This work also made use of the Rainbow Cosmological Surveys Database, which is operated by the Centro de Astrobiología (CAB/INTA), partnered with the University of California Observatories at Santa Cruz (UCO/Lick,UCSC).

We also acknowledge support from the National Natural Science Foundation of China (12073003, 12150410307, 12003003, 11721303, 11991052, 11950410493) and the China Manned Space Project Nos. CMS-CSST-2021-A04 and CMS-CSST-2021-A06. P.G.P.-G. acknowledges support from Spanish Ministerio de Ciencia e Innovación MCIN/AEI/10.13039/501100011033 through grant PGC2018-093499-B-I00.

A.G. acknowledges financial contribution from the grant PRIN INAF 2019 (RIC) 1.05.01.85.09, "New Light on the Intergalactic Medium (NewIGM)," and support from PRIN MIUR project "Black Hole Winds and the Baryon Life Cycle of Galaxies: The Stone-Guest at the Galaxy Evolution Supper," contract 2017-PH3WAT.

Appendix
Additional NIRSpec Spectra of CEERS 2782 and CEERS 746

In this appendix, we present additional spectra of CEERS 2782 and CEERS 746 taken with NIRSpec. Figures 11 and 12 display the spectra of both sources in the G140M/F100LP and G235M/F170LP grating and filter combinations, which cover the wavelength ranges 0.97–1.84 μm and 1.66–3.07 μm, respectively. These shorter-wavelength spectra provide access to rest-frame UV lines with high ionization potentials, such as [Ne V] λ3427, which have been used as tracers of AGN activity (e.g., Cleri et al. 2023). The expected locations of [Ne V] and C III] λ1909 (CEERS 746 only) are noted in the spectra; however, neither line is detected.

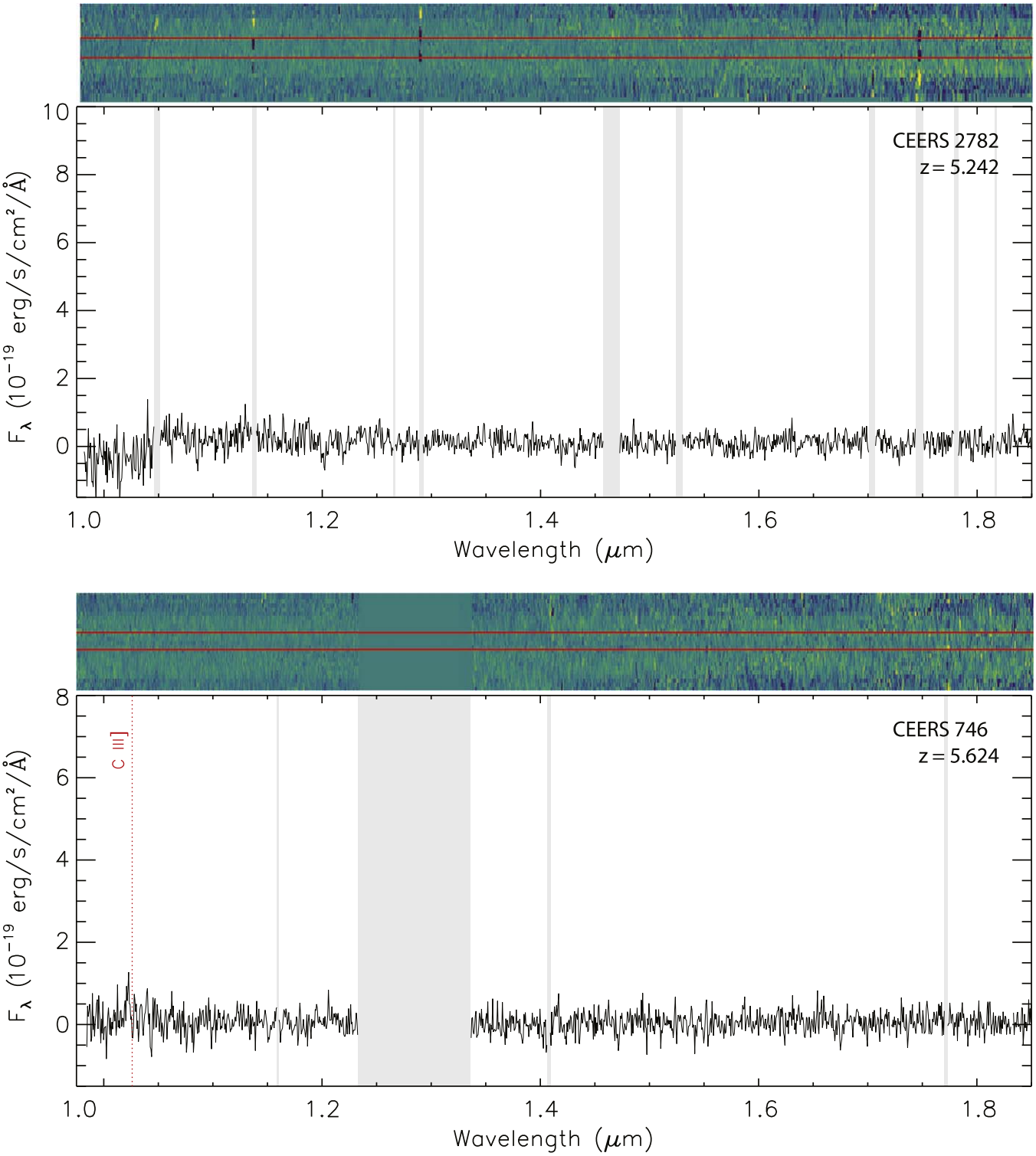

Figure 11. NIRSpec spectra of sources CEERS 2782 and CEERS 746 taken in the G140M grating with $R \sim 1000$. The 2D spectra are shown above, with extraction windows highlighted in red. Gray regions in both the 1D and 2D spectra indicate regions masked owing to artifacts identified via visual inspection and the detector chip gap. The expected locations of notable emission lines, both detected and not detected, are noted.

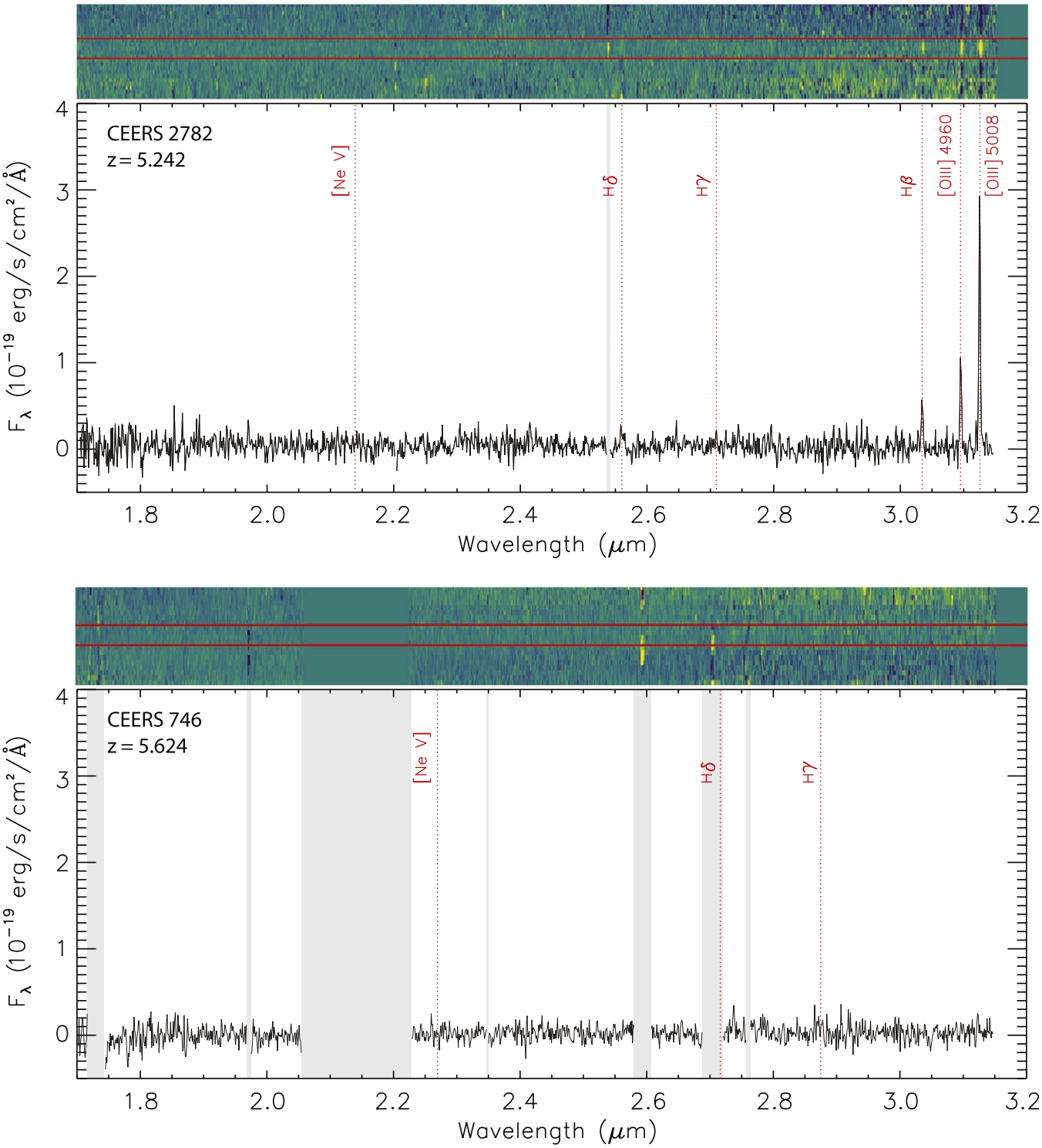

Figure 12. NIRSpec spectra of sources CEERS 2782 and CEERS 746 taken in the G235M grating with $R \sim 1000$. The 2D spectra are shown above, with extraction windows highlighted in red. Gray regions in both the 1D and 2D spectra indicate regions masked owing to artifacts identified via visual inspection and the detector chip gap. The expected locations of notable emission lines, both detected and not detected, are noted.

ORCID iDs

Dale D. Kocevski https://orcid.org/0000-0002-8360-3880
Masafusa Onoue https://orcid.org/0000-0003-2984-6803
Kohei Inayoshi https://orcid.org/0000-0001-9840-4959
Jonathan R. Trump https://orcid.org/0000-0002-1410-0470
Pablo Arrabal Haro https://orcid.org/0000-0002-7959-8783
Andrea Grazian https://orcid.org/0000-0002-5688-0663
Mark Dickinson https://orcid.org/0000-0001-5414-5131
Steven L. Finkelstein https://orcid.org/0000-0001-8519-1130
Jeyhan S. Kartaltepe https://orcid.org/0000-0001-9187-3605
Michaela Hirschmann https://orcid.org/0000-0002-3301-3321
James Aird https://orcid.org/0000-0003-1908-8463
Benne W. Holwerda https://orcid.org/0000-0002-4884-6756
Seiji Fujimoto https://orcid.org/0000-0001-7201-5066
Stéphanie Juneau https://orcid.org/0000-0002-0000-2394
Ricardo O. Amorín https://orcid.org/0000-0001-5758-1000
Bren E. Backhaus https://orcid.org/0000-0001-8534-7502
Micaela B. Bagley https://orcid.org/0000-0002-9921-9218
Guillermo Barro https://orcid.org/0000-0002-0786-7307
Eric F. Bell https://orcid.org/0000-0002-5564-9873
Laura Bisigello https://orcid.org/0000-0003-0492-4924
Antonello Calabrò https://orcid.org/0000-0003-2536-1614
Nikko J. Cleri https://orcid.org/0000-0001-7151-009X
M. C. Cooper https://orcid.org/0000-0003-1371-6019
Xuheng Ding https://orcid.org/0000-0001-8917-2148
Norman A. Grogin https://orcid.org/0000-0001-9440-8872
Luis C. Ho https://orcid.org/0000-0001-6947-5846
Taylor A. Hutchison https://orcid.org/0000-0001-6251-4988
Akio K. Inoue https://orcid.org/0000-0002-7779-8677
Linhua Jiang https://orcid.org/0000-0003-4176-6486
Anton M. Koekemoer https://orcid.org/0000-0002-6610-2048
Wenxiu Li https://orcid.org/0000-0002-1044-4081
Zhengrong Li https://orcid.org/0000-0002-8502-7573
Elizabeth J. McGrath https://orcid.org/0000-0001-8688-2443
Juan Molina https://orcid.org/0000-0002-8136-8127
Casey Papovich https://orcid.org/0000-0001-7503-8482
Pablo G. Pérez-González https://orcid.org/0000-0003-4528-5639
Nor Pirzkal https://orcid.org/0000-0003-3382-5941
Stephen M. Wilkins https://orcid.org/0000-0003-3903-6935
Guang Yang https://orcid.org/0000-0001-8835-7722
L. Y. Aaron Yung https://orcid.org/0000-0003-3466-035X

References

Adams, N. J., Bowler, R. A. A., Jarvis, M. J., Varadaraj, R. G., & Häußler, B. 2023, MNRAS, 523, 327
Aird, J., Coil, A. L., & Georgakakis, A. 2018, MNRAS, 474, 1225
Alexandroff, R. M., Zakamska, N. L., Barth, A. J., et al. 2018, MNRAS, 479, 4936
Amorín, R., Pérez-Montero, E., Vílchez, J. M., & Papaderos, P. 2012, ApJ, 749, 185
Backhaus, B. E., Trump, J. R., Cleri, N. J., et al. 2022, ApJ, 926, 161
Bagley, M. B., Finkelstein, S. L., Koekemoer, A. M., et al. 2023, ApJL, 946, 23
Baldassare, V. F., Reines, A. E., Gallo, E., & Greene, J. E. 2015, ApJL, 809, L14
Baldwin, J. A., Phillips, M. M., & Terlevich, R. 1981, PASP, 93, 5
Bañados, E., Venemans, B. P., Decarli, R., et al. 2016, ApJS, 227, 11
Bennert, V. N., Auger, M. W., Treu, T., Woo, J.-H., & Malkan, M. A. 2011, ApJ, 742, 107
Bertin, E., & Arnouts, S. 1996, A&AS, 117, 393
Bouwens, R. J., Oesch, P. A., Stefanon, M., et al. 2021, AJ, 162, 47
Bowler, R. A. A., Adams, N. J., Jarvis, M. J., & Häußler, B. 2021, MNRAS, 502, 662
Brammer, G. B., van Dokkum, P. G., Franx, M., et al. 2012, ApJS, 200, 13
Bruzual, G., & Charlot, S. 2003, MNRAS, 344, 1000
Bushouse, H., Eisenhamer, J., Dencheva, N., et al. 2022, spacetelescope/jwst v1.5.3, Zenodo, doi:10.5281/zenodo.6984365
Calzetti, D., Armus, L., Bohlin, R. C., et al. 2000, ApJ, 533, 682
Carnall, A. C., McLure, R. J., Dunlop, J. S., et al. 2023, arXiv:2301.11413
Casertano, S., de Mello, D., Dickinson, M., et al. 2000, AJ, 120, 2747
Chabrier, G. 2003, PASP, 115, 763
Cleri, N. J., Olivier, G. M., Hutchison, T. A., et al. 2023, arXiv:2301.07745
Dickey, J. M., & Lockman, F. J. 1990, ARA&A, 28, 215
Ding, X., Onoue, M., Silverman, J. D., et al. 2022a, arXiv:2211.14329
Ding, X., Silverman, J., Treu, T., et al. 2020, ApJ, 888, 37
Ding, X., Silverman, J. D., & Onoue, M. 2022b, ApJL, 939, L28
Erb, D. K., Shapley, A. E., Pettini, M., et al. 2006, ApJ, 644, 813
Faisst, A. L., Chary, R. R., Fajardo-Acosta, S., et al. 2022, ApJ, 929, 66
Fan, X., Banados, E., & Simcoe, R. A. 2022, arXiv:2212.06907
Fan, X., Narayanan, V. K., Lupton, R. H., et al. 2001, AJ, 122, 2833
Feltre, A., Charlot, S., & Gutkin, J. 2016, MNRAS, 456, 3354
Ferrarese, L., & Merritt, D. 2000, ApJL, 539, L9
Finkelstein, S. L., & Bagley, M. B. 2022a, ApJ, 938, 25
Finkelstein, S. L., & Bagley, M. B. 2022b, ApJ, 938, 17
Finkelstein, S. L., Bagley, M. B., Arrabal Haro, P., et al. 2022, ApJL, 940, 15
Finkelstein, S. L., D'Aloisio, A., Paardekooper, J.-P., et al. 2019, ApJ, 879, 36
Fruchter, A. S., & Hook, R. N. 2002, PASP, 114, 144
Fujimoto, S., Brammer, G. B., Watson, D., et al. 2022, Natur, 604, 261
Furtak, L. J., Zitrin, A., Plat, A., et al. 2023, ApJ, 952, 14
Gebhardt, K., Bender, R., Bower, G., et al. 2000, ApJL, 539, L13
Giallongo, E., Grazian, A., Fiore, F., et al. 2015, A&A, 578, A83
Giallongo, E., Grazian, A., Fiore, F., et al. 2019, ApJ, 884, 19
Grazian, A., Giallongo, E., Boutsia, K., et al. 2022, ApJ, 924, 62
Grazian, A., Giallongo, E., Fiore, F., et al. 2020, ApJ, 897, 94
Greene, J. E., Alexandroff, R., Strauss, M. A., et al. 2014, ApJ, 788, 91
Greene, J. E., & Ho, L. C. 2005, ApJ, 630, 122
Greene, J. E., & Ho, L. C. 2007, ApJ, 670, 92
Gregg, M. D., Lacy, M., White, R. L., et al. 2002, ApJ, 564, 133
Grogin, N. A., Kocevski, D. D., Faber, S. M., et al. 2011, ApJS, 197, 35
Groves, B. A., Heckman, T. M., & Kauffmann, G. 2006, MNRAS, 371, 1559
Habouzit, M., Onoue, M., Bañados, E., et al. 2022, MNRAS, 511, 3751
Harikane, Y., Ono, Y., Ouchi, M., et al. 2022, ApJS, 259, 20
Hirschmann, M., Charlot, S., Feltre, A., et al. 2019, MNRAS, 487, 333
Hirschmann, M., Charlot, S., Feltre, A., et al. 2022, arXiv:2212.02522
Hirschmann, M., Khochfar, S., Burkert, A., et al. 2010, MNRAS, 407, 1016
Hogarth, L., Amorín, R., Vílchez, J. M., et al. 2020, MNRAS, 494, 3541
Hu, H., Inayoshi, K., Haiman, Z., et al. 2022, ApJ, 935, 140
Inayoshi, K., Nakatani, R., Toyouchi, D., et al. 2022a, ApJ, 927, 237
Inayoshi, K., Onoue, M., Sugahara, Y., Inoue, A. K., & Ho, L. C. 2022b, ApJL, 931, L25
Inayoshi, K., Visbal, E., & Haiman, Z. 2020, ARA&A, 58, 27
Izumi, T., Matsuoka, Y., Fujimoto, S., et al. 2021, ApJ, 914, 36
Izumi, T., Onoue, M., Matsuoka, Y., et al. 2019, PASJ, 71, 111
Jiang, L., McGreer, I. D., Fan, X., et al. 2016, ApJ, 833, 222
Jiang, L., Ning, Y., Fan, X., et al. 2022, NatAs, 6, 850
Kaspi, S., Smith, P. S., Netzer, H., et al. 2000, ApJ, 533, 631
Kato, N., Matsuoka, Y., Onoue, M., et al. 2020, PASJ, 72, 84
Kauffmann, G., Heckman, T. M., Tremonti, C., et al. 2003, MNRAS, 346, 1055
Kewley, L. J., Dopita, M. A., Leitherer, C., et al. 2013a, ApJ, 774, 100
Kewley, L. J., Maier, C., Yabe, K., et al. 2013b, ApJL, 774, L10
Kewley, L. J., Nicholls, D. C., Sutherland, R., et al. 2019, ApJ, 880, 16
Kim, D., Im, M., Glikman, E., Woo, J.-H., & Urrutia, T. 2015, ApJ, 812, 66
Kim, Y., & Im, M. 2021, ApJL, 910, L11
Kim, Y., Im, M., Jeon, Y., et al. 2018, ApJ, 855, 138
Kim, Y., Im, M., Jeon, Y., et al. 2020, ApJ, 904, 111
Kocevski, D. D., Barro, G., McGrath, E. J., et al. 2023, ApJL, 946, L14
Koekemoer, A. M., Faber, S. M., Ferguson, H. C., et al. 2011, ApJS, 197, 36
Kormendy, J., & Ho, L. C. 2013, ARA&A, 51, 511
Kraft, R. P., Burrows, D. N., & Nousek, J. A. 1991, ApJ, 374, 344

Kriek, M., van Dokkum, P. G., Franx, M., Illingworth, G. D., & Magee, D. K. 2009, ApJL, 705, L71
Labbe, I., van Dokkum, P., Nelson, E., et al. 2023, Natur, 616, 266
Larson, R. L., Finkelstein, S. L., Kocevski, D. D., et al. 2023, arXiv:2303.08918
Li, W., Inayoshi, K., Onoue, M., & Toyouchi, D. 2023, ApJ, 950, L85
Liu, D., Daddi, E., Dickinson, M., et al. 2018, ApJ, 853, 172
Liu, H.-Y., Liu, W.-J., Dong, X.-B., et al. 2019, ApJS, 243, 21
Liu, X., Shapley, A. E., Coil, A. L., Brinchmann, J., & Ma, C.-P. 2008, ApJ, 678, 758
Magorrian, J., Tremaine, S., Richstone, D., et al. 1998, AJ, 115, 2285
Maraston, C., Pforr, J., Renzini, A., et al. 2010, MNRAS, 407, 830
Markwardt, C. B. 2009, in ASP Conf. Ser. 411, Astronomical Data Analysis Software and Systems XVIII, ed. D. A. Bohlender, D. Durand, & P. Dowler (San Francisco, CA: ASP), 251
Matsuoka, Y., Iwasawa, K., Onoue, M., et al. 2022, ApJS, 259, 18
Matsuoka, Y., Onoue, M., Kashikawa, N., et al. 2016, ApJ, 828, 26
Matsuoka, Y., Onoue, M., Kashikawa, N., et al. 2019, ApJL, 872, L2
Matsuoka, Y., Strauss, M. A., Kashikawa, N., et al. 2018, ApJ, 869, 150
Mazzucchelli, C., Bañados, E., Venemans, B. P., et al. 2017, ApJ, 849, 91
McConnell, N. J., & Ma, C.-P. 2013, ApJ, 764, 184
McGreer, I. D., Fan, X., Jiang, L., & Cai, Z. 2018, AJ, 155, 131
Mezcua, M., Civano, F., Marchesi, S., et al. 2018, MNRAS, 478, 2576
Miller, B. P., Gallo, E., Greene, J. E., et al. 2015, ApJ, 799, 98
Molina, M., Reines, A. E., Latimer, L. J., Baldassare, V., & Salehirad, S. 2021, ApJ, 922, 155
Momcheva, I. G., Brammer, G. B., van Dokkum, P. G., et al. 2016, ApJS, 225, 27
Nakajima, K., & Maiolino, R. 2022, MNRAS, 513, 5134
Nandra, K., Laird, E. S., Aird, J. A., et al. 2015, ApJS, 220, 10
Neeleman, M., Novak, M., Venemans, B. P., et al. 2021, ApJ, 911, 141
Nicholls, D. C., Sutherland, R. S., Dopita, M. A., Kewley, L. J., & Groves, B. A. 2017, MNRAS, 466, 4403
Niida, M., Nagao, T., Ikeda, H., et al. 2020, ApJ, 904, 89
Onoue, M., Inayoshi, K., Ding, X., et al. 2023, ApJL, 942, L17
Onoue, M., Kashikawa, N., Matsuoka, Y., et al. 2019, ApJ, 880, 77
Onoue, M., Kashikawa, N., Willott, C. J., et al. 2017, ApJL, 847, L15
Osterbrock, D. E. 1989, Astrophysics of Gaseous Nebulae and Active Galactic Nuclei (Mill Valley, CA: Univ. Science Books)
Park, D., Woo, J.-H., Bennert, V. N., et al. 2015, ApJ, 799, 164
Peng, C. Y., Ho, L. C., Impey, C. D., & Rix, H.-W. 2002, AJ, 124, 266
Pérez-González, P. G., Barro, G., Annunziatella, M., et al. 2023, ApJL, 946, 24
Polletta, M., Tajer, M., Maraschi, L., et al. 2007, ApJ, 663, 81
Polletta, M. d. C., Wilkes, B. J., Siana, B., et al. 2006, ApJ, 642, 673
Reed, S. L., McMahon, R. G., Banerji, M., et al. 2015, MNRAS, 454, 3952
Reines, A. E., Greene, J. E., & Geha, M. 2013, ApJ, 775, 116
Reines, A. E., & Volonteri, M. 2015, ApJ, 813, 82
Ricarte, A., & Natarajan, P. 2018, MNRAS, 481, 3278
Richards, G. T., Lacy, M., Storrie-Lombardi, L. J., et al. 2006, ApJS, 166, 470
Rigby, J., Perrin, M., McElwain, M., et al. 2023, PASP, 35, 31
Sanders, R. L., Shapley, A. E., Jones, T., et al. 2023, ApJ, 942, 24
Schmidt, E. O., Ferreiro, D., Vega Neme, L., & Oio, G. A. 2016, A&A, 596, A95
Scoggins, M. T., Haiman, Z., & Wise, J. H. 2023, MNRAS, 519, 2155
Shapley, A. E., Coil, A. L., Ma, C.-P., & Bundy, K. 2005, ApJ, 635, 1006
Shen, Y., Wu, J., Jiang, L., et al. 2019, ApJ, 873, 35
Shimasaku, K., & Izumi, T. 2019, ApJL, 872, L29
Silva, L., Maiolino, R., & Granato, G. L. 2004, MNRAS, 355, 973
Somerville, R. S., Hopkins, P. F., Cox, T. J., Robertson, B. E., & Hernquist, L. 2008, MNRAS, 391, 481
Storchi-Bergmann, T., Schmitt, H. R., Calzetti, D., & Kinney, A. L. 1998, AJ, 115, 909
Storey, P. J., & Zeippen, C. J. 2000, MNRAS, 312, 813
Suh, H., Civano, F., Trakhtenbrot, B., et al. 2020, ApJ, 889, 32
Sun, M., Trump, J. R., Brandt, W. N., et al. 2015, ApJ, 802, 14
Tanaka, T., & Haiman, Z. 2009, ApJ, 696, 1798
Trakhtenbrot, B., & Netzer, H. 2010, MNRAS, 406, L35
Trakhtenbrot, B., Netzer, H., Lira, P., & Shemmer, O. 2011, ApJ, 730, 7
Trump, J. R., Arrabal Haro, P., Simons, R. C., et al. 2023, ApJ, 945, 11
Trump, J. R., Sun, M., Zeimann, G. R., et al. 2015, ApJ, 811, 26
Übler, H., Maiolino, R., Curtis-Lake, E., et al. 2023, arXiv:2302.06647
Valiante, R., Schneider, R., Volonteri, M., & Omukai, K. 2016, MNRAS, 457, 3356
Vanden Berk, D. E., Richards, G. T., Bauer, A., et al. 2001, AJ, 122, 549
Venemans, B. P., Walter, F., Zschaechner, L., et al. 2016, ApJ, 816, 37
Volonteri, M. 2010, A&ARv, 18, 279
Volonteri, M., Habouzit, M., & Colpi, M. 2021, NatRP, 3, 732
Volonteri, M., Lodato, G., & Natarajan, P. 2008, MNRAS, 383, 1079
Volonteri, M., & Natarajan, P. 2009, MNRAS, 400, 1911
Wang, F., Yang, J., Fan, X., et al. 2021, ApJL, 907, L1
Wang, R., Wagg, J., Carilli, C. L., et al. 2013, ApJ, 773, 44
Willott, C. J., Albert, L., Arzoumanian, D., et al. 2010, AJ, 140, 546
Willott, C. J., Bergeron, J., & Omont, A. 2017, ApJ, 850, 108
Willott, C. J., Delorme, P., Omont, A., et al. 2007, AJ, 134, 2435
Yang, J., Fan, X., Gupta, A., et al. 2023, arXiv:2302.01777
York, D. G., Adelman, J., Anderson, J. E. J., et al. 2000, AJ, 120, 1579
Yung, L. Y. A., Somerville, R. S., Finkelstein, S. L., et al. 2021, MNRAS, 508, 2706
Zakamska, N. L., Schmidt, G. D., Smith, P. S., et al. 2005, AJ, 129, 1212
Zavala, J. A., Aretxaga, I., Geach, J. E., et al. 2017, MNRAS, 464, 3369